Effect of Zirconium as Dopant in $NaFePO_4$ as Cathode for Sodium ion Batteries

By

GAYATHIRI D

(Reg.No. 20PPH007)

Supervisor

Dr.B.Nalini

Department of Physics

A Thesis submitted to

Avinashilingam Institute for Home Science and Higher Education for Women,

Coimbatore-641 043

In Partial Fulfilment of the Requirements for the Degree of

MASTER OF SCIENCE IN PHYSICS

MAY 2022

Effect of Zirconium as Dopant in $NaFePO_4$ as Cathode for Sodium ion Batteries

By

GAYATHIRI D

(Reg.No. 20PPH007)

Supervisor

Dr.B.Nalini

Department of Physics

A Thesis submitted to

Avinashilingam Institute for Home Science and Higher Education for Women,

Coimbatore-641 043

In partial fulfilment of the requirements for the degree of

MASTER OF SCIENCE IN PHYSICS

MAY 2022

CERTIFIED AS A BONAFIED RESEARCH WORK

27/05/22

Signature of Head of the Department

27/05/2022

Signature of the Supervisor

ACKNOWLEDGEMENT

I owe my sincere thanks to Lord Almighty and my parents for showering their generous blessings upon me in all endeavous.

I wish to express my gratitude to our chancellor, **Prof S.P.Thyagarajan,** Avinashilingam Institute for Home Science and Higher Education for Women, Coimbatore for providing all facilities to conduct this study.

I extend my thanks to **Dr. (Mrs) V.Bharathi Harishankar,** Ph.D., FRSA, Vice Chancellor, Avinashilingam Institute for Home Science and Higher Education for Women, Coimbatore, for providing flamboyant help towards the completion of the study.

I record my deep sense of gratitude and indebtedness to **Dr. (Mrs) S.Kowsalya,** M.Sc.,M.Phil., Ph.D., Registrar, Avinashilingam Institute for Home Science and Higher Education for Women, Coimbatore, for timely help rendered throughout the course of this work.

I am also thankful to **Dr. (Mrs) G.Padmavathi,** M.Sc., M.Phil., Ph.D., Dean, School of Physical Sciences and Computational Sciences, Avinashilingam Institute for Home Science and Higher Education for Women, Coimbatore, for granting the facilities required.

I whole heartily thank to **Dr. (Mrs)J.Shanthi**, M.Sc., M.Phil., Ph.D., Professor and Head of the Department of Physics, Avinashilingam Institute for Home Science and Higher Education for Women, Coimbatore, for her encouragement and generous help which was of great value.

I am also thanks to Dr. **(Mrs.) N. S. Rajeswari,** M.Sc., M.Phil., M.C.A., SLET, Ph.D.,Assistant Professor-SG and former Head of the Department of Physics, Avinashilingam Institute for Home Science and Higher Education for Women, Coimbatore for her help and support.

I express my heartiest thanks to my guide **Dr. (Mrs)B.Nalini**, M.Sc., Ph.D., M.S(Edu.Mgt), STA fellow, AIST Fellow (Japan), Assistant Professor, Department of Physics, Avinashilingam Institute for Home Science and Higher Education for Women, Coimbatore, for her inspiring

guidance, meticulous care, patience, help, encouragement and motivation.

I express my gratitude to **(Mrs)P.Priyanka** and **(Mrs)G.G.Soundarya**, Research Scholar, Department of Physics, Avinashilingam Institute for Home Science and Higher Education for Women, Coimbatore, for their valuable help in completion of my project.

I wish to express my special thanks to my parents, my friends and all my well-wishers for their constant encouragement, support and help in carrying out this work.

D.GAYATHIRI

(20PPH007)

DECLARATION

I hereby declare that the project work entitled "**Effect of Zirconium as dopant in $NaFePO_4$ as cathode for sodium ion batteries**" submitted to the Department of Physics, Avinashilingam Institute for Home Science and Higher Education for Women, Coimbatore, is a record of an original work done by me under the guidance of **Dr. (Mrs)B.Nalini,** Assistant Professor, Department of Physics, and the project work is submitted in the fulfilment of the requirements for the degree of Master of Science in Physics. The results embodied in this have not been submitted to any other university or institute for the award of any degree or diploma.

D. Gayathiri

GAYATHIRI D

(20PPH007)

LIST OF CONTENTS

LIST OF TABLES

LIST OF FIGURES

CHAPTER I

INTRODUCTION

Energy storage technology has received significant attention for portable electronic devices, electric vehicle propulsion, bulk electricity storage at power stations, and load levelling of renewable sources, such as solar energy and wind power. Lithium ion batteries have dominated most of the first two applications. However, moving beyond lithium batteries the element that lies below sodium is a sensible step that offers sustainability and cost-effectiveness. Sodium-ion batteries don't have the same high energy density as lithium-ion and they won't last for quite as long on each charge. One big advantage of sodium ion vs lithium-ion is that the lower price and reduced environmental impact. Sodium-ion batteries could be a viable alternative to lithium-ion batteries [1].

1.1 Electrochemical energy storage device

The increasing demand for environmental friendly portable devices and electric vehicles also requires higher efficiency and more reliable energy storage devices based on the current rechargeable batteries and supercapacitors. The electrochemical energy storage devices utilize reversible electrochemical energy via the simultaneous flow of both electrons and ions. Flexible materials can be used in wearable devices for the applications in energy storage and supercapacitors [2].

1.2 Energy storage device applications

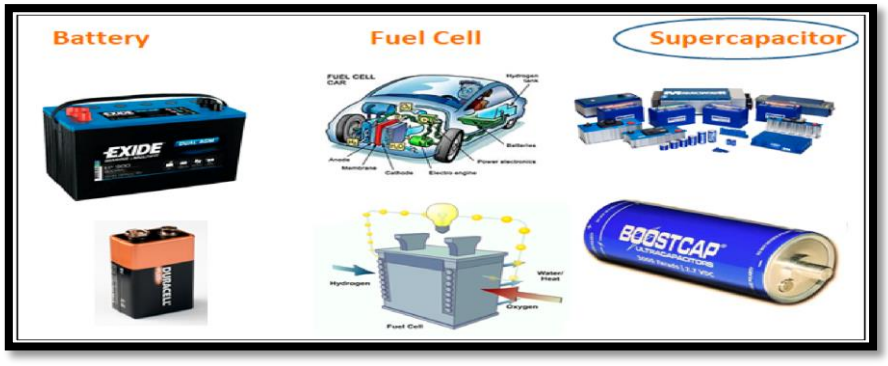

Figure 1.1: Types of electrochemical energy storage devices.

The prerequisite for storing energy to explore more and more inexpensive techniques for energy storage. Storing energy electrochemically using electrochemical energy storage devices

like fuel cells, batteries, and supercapacitors having a different mechanism of energy storage but have electrochemical resemblances.

Battery and supercapacitors are most commonly used energy storage devices, but fuel cell does not store energy instead produces energy directly from the fuel via oxygen electrochemical reactions in the cell.

1.2.1 Batteries

A battery is a collection of one or more cells that go under chemical reactions to create the flow of electrons within a circuit.

A battery is one or more electrically connected electrochemical cells having terminals/contacts to supply electrical energy.

Battery cells are usually made up of three main components;

1. The Anode (Negative Electrode)
2. The Cathode (Positive Electrode)
3. The electrolytes

Anode-The anode is the negative electrode of a cell associated with oxidative chemical reactions that release electrons into the external circuit.

Cathode-The cathode is the positive electrode of a cell associated with reductive chemical reactions that gain electrons from the external circuit.

Electrolyte-An electrolyte is a material that provides pure ionic conductivity between the positive and negative electrodes of a cell.

Separator-A separator is a physical barrier between the positive and negative electrodes incorporated into most cell designs to prevent electrical shorting [3].

1.3 History of batteries

American scientist and inventor Benjamin Franklin first used the term "battery" in 1749 when he was doing experiments with electricity using a set of linked capacitors. The first true battery was invented by the Italian physicist Alessandro Volta in 1800. Volta stacked discs of copper (Cu) and zinc (Zn) separated by cloth soaked in salty water. Wires connected to either

end of the stack produced a continuous stable current. Each cell produces 0.76 Volts (V). A multiple of this value is obtained given by the number of cells that are stacked together. One of the most enduring batteries, the lead-acid battery, was invented in 1859 and is still the technology used to start most internal combustion engine cars today. It is the oldest example of rechargeable battery [4].

1.4 Types of batteries

Batteries generally can be classified into two types

1. Primary Batteries
2. Secondary Batteries

1.4.1 Primary batteries

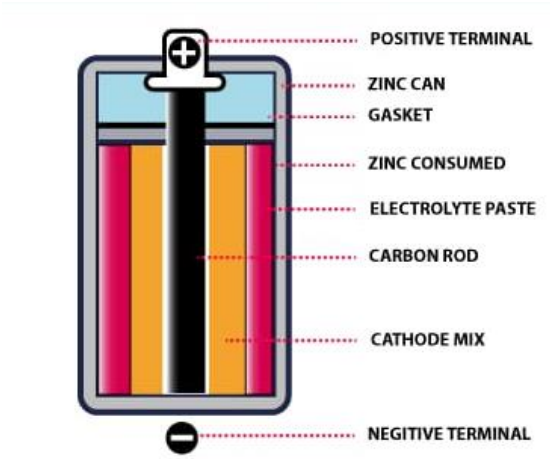

Figure 1.2: Primary cell

- Primary batteries are batteries that **cannot be recharged** once depleted. Primary batteries are made of electrochemical cells whose electrochemical reaction cannot be reversed.

- Primary batteries exist in different forms **ranging from coin cells to AA batteries**. They are commonly used in standalone applications where charging is impractical or impossible. A good example of which is in military grade devices and battery powered equipment. It will be impractical to use rechargeable batteries as recharging a battery will be the last thing in the mind of the soldiers.

- Primary batteries always have high specific energy and the systems in which they are used are always designed to consume low amount of power to enable the battery last as long as possible. The most popular type of primary batteries are **alkaline batteries**. They have a high specific energy and are environmental friendly, cost-effective and do not leak even when fully discharged [5].

There are Two Main Types of Primary Cells

1. **Alkaline Batteries**

Chemical composition of Zinc with Manganese dioxide forms these batteries. The electrolyte that is used in these types of batteries is potassium hydroxide and since all the contents are purely alkaline, it is termed as an alkaline battery.

2. **Coin Cell Batteries**

The coin cell batteries also have alkaline electrolytes, and additionally, they also have the chemicals of lithium and silver oxides. These types of primary batteries are highly efficient in ensuring stable and steady voltage.

1.4.2 Secondary batteries

- Secondary batteries are batteries with electrochemical cells whose chemical reactions can be reversed by applying a certain voltage to the battery in the reversed direction. Also referred to as **rechargeable batteries**, secondary cells unlike primary cells can be recharged after the energy on the battery has been used up.

- Small capacity secondary batteries are used to power portable electronic devices like **mobile phones** and other gadgets and appliances while heavy-duty batteries are used in powering diverse **electric vehicles** and other high drain applications like load levelling in electricity generation.

- Although the initial cost of acquiring rechargeable batteries is always a whole lot higher than that of primary batteries but they are the most cost-effective over the long-term.

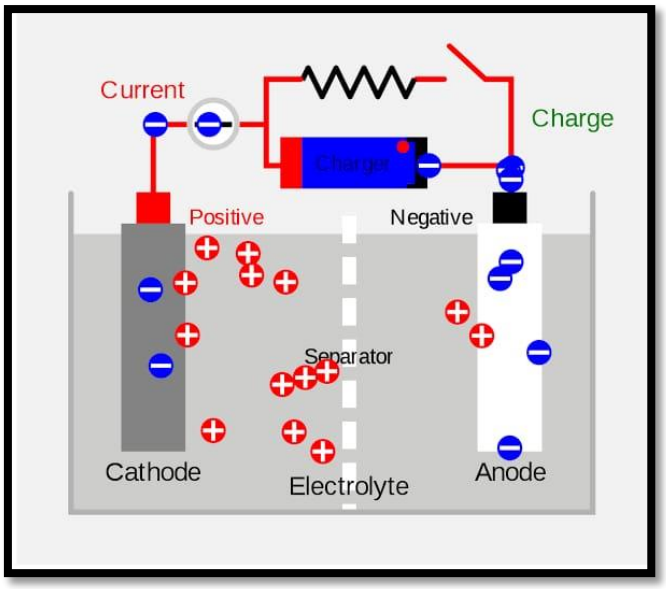

Figure 1.3 Secondary battery

Types of Secondary batteries are**,**

- **Lead-acid Batteries**

These batteries contain lead-acid that is cheaper and used mostly in vehicles.

- **Nickel-cadmium (Ni-Cd) Battery**

This type of battery is made of Nickel and Cadmium. It has a lower price, and has a lower discharge rate.

- **Nickel Metal Hydrate (Ni-MH) Battery**

These batteries are more preferred than Ni-Cd ones.

- **Li-ion Battery**

These batteries are made up of Lithium metal. They are compact and can easily be used in portable devices.

- **Lithium Polymer battery**

These batteries are also known as Lithium-ion Polymer batteries as they use polymer gel or electrolyte instead of liquid ones. These batteries are a bit costlier but are highly protected as compared to the Li-ion batteries [6].

1.5 Prevailing battery technologies

Batteries have become a prevalent energy source for applications in the world today. Rechargeable batteries are normally managed by a battery management system. The battery management system takes information from the battery in order to provide estimates and useful safety features. New funding in battery technology has led to recent innovations, performance benefits, and reduced costs. New battery technologies are

- Lithium-ion batteries
- Lithium-Sulfur batteries
- Sodium ion batteries [7]

Due to the limiting factors of Lithium ion batteries, an alternate technology is under research, in this way Sodium ion batteries could be a better option and hence preparation of cathode material and its properties is studied in this work.

1.6 Sodium-ion batteries

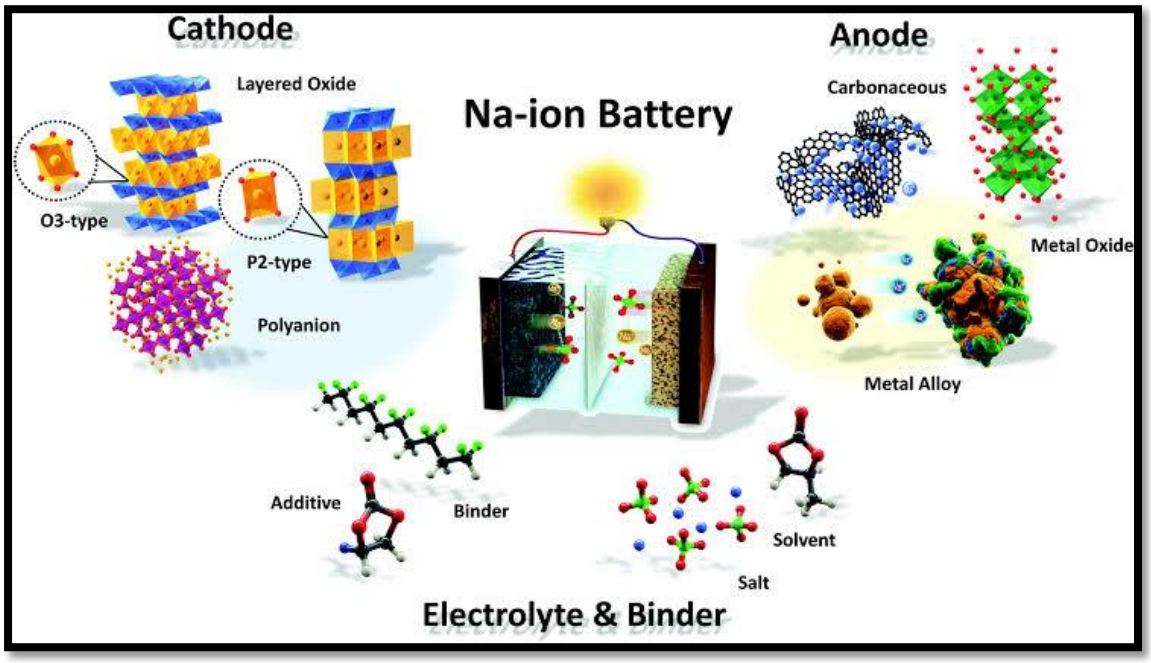

Figure 1.4: Recent advances in phosphate cathode material for sodium ion batteries.

- Sodium-ion battery (SIB) was originally developed in the late 1980s, in approximately the same time period as LIB.

- SIB was ignored after commercialization LIB was invented successfully. Recently, SIB has attracted great attention due to the abundant sodium resources in the Earth's crust and low cost.
- Lithium ion batteries are used in most mobile electronic devices as well as in zero-emission electronic vehicles.
- However, there are increasing concerns regarding load leveling of renewable energy sources and the smart grid as well as the **sustainability of lithium sources due to their limited availability and consequent expected price increase.**
- Therefore, whether lithium ion batteries alone can satisfy the rising demand for small- and/or mid-to-large-format energy storage applications remains unclear.
- To mitigate these issues, recent research has focused on alternative energy storage systems.
- Sodium-ion batteries are considered as the best candidate power sources because sodium is widely available and exhibits similar chemistry to that of lithium ion batteries; therefore, Sodium ion batteries are promising next-generation alternatives.
- Recently, **sodiated layer** transition metal oxides, phosphates and organic compounds have been introduced as **cathode materials for Sodium ion batteries** [8].

1.6.1 Basic concepts

- A typical sodium-ion battery consists of anode, cathode, electrolyte (nonaqueous/aqueous) and a separator.
- The operation is similar to that of Lithium ion batteries.
- **The sodium ions are transferred to the negative electrode through the electrolyte with the active material**.
- The electrons are pushed from cathode to anode through the external circuit during charging process.
- Accordingly, an oxidation and reduction reaction takes place at the respective electrode.
- The cell voltage increases as the cell is charged [9]

1.6.2 Cathode Materials for Na- ion Battery

Sodium-ion cathode materials are typically based on intercalation / de-intercalation compounds, where sodium ions provided by the cathode are inserted into the host lattice during charge and extracted during discharge, with minimal structural change in the host material.

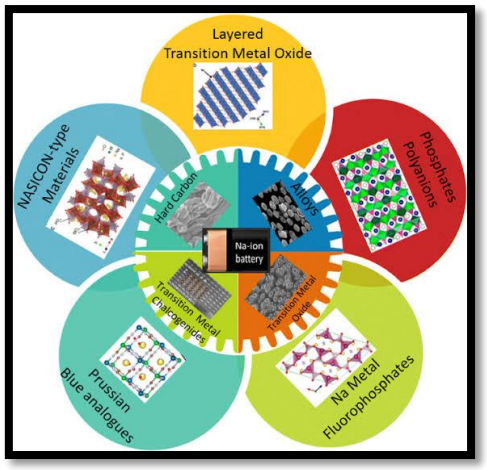

Figure 1.5: Electrode materials for sodium ion batteries

The most common cathodes for SIBs are,

- Sodium oxides ($NaMO_2$, M = V, Fe, Mn, Cu, Co., and Ni), Sodium phosphates ($Na_7V_3(P_2O_7)_4$, $NaFePO_4$, Transition metal oxides (V_2O_5) and Prussian blue (PB, $Na_2M[Fe(CN)_6]$) [10]
- Variety of cathode compounds for sodium ion batteries have been found. They are mainly categorized into layered oxides and polyanionic compounds ($NaFePO_4$). Due to the long cycling life, stable three dimensional polyanionic framework and its safety, Sodium ion phosphate ($NaFePO_4$) is considered as cathode material for sodium ion battery.

1.6.3 Advantages of Na-ion batteries

The sodium salt raw material reserves are abundant and the price is low. Due to the characteristics of sodium salt, it is allowed to use low-concentration electrolyte to reduce costs. Since the sodium-ion battery has no over-discharge characteristics, the sodium-ion battery is allowed to discharge to zero volts [11].

1.7 Objective:

To analyze the effect of Zirconium as dopant in $NaFePO_4$ as cathode for sodium ion batteries.

1.8 Approach:

- To prepare the samples $NaFePO_4$ and $NaFe_{0.98}Zr_{0.02}PO_4$ by sol-gel method.
- To characterize the prepared samples by structural, morphological, and electrochemical studies.

CHAPTER II

REVIEW OF LITERATURE

$NaFePO_4$ as a cathode material for sodium ion batteries

Highly dispersed maricite $NaFePO_4$ nanoclusters with ultrafine NaFePO4@C subunits have been synthesized by **Liu et al., (2021) [12] by** facile method. Ex situ X-Ray Diffraction (XRD) was used to further investigate Na-storage mechanism of maricite $NaFePO_4$ nanoclusters. Raman spectroscopy was tested to evaluate defect level in carbon of NaFePO4 sample, exhibits two characteristic bands at 1595.3 cm^{-1} (G-band) and 1351.7 cm^{-1} (D band), corresponding to graphitic and disordered structures, respectively. Scanning Electron Microscopy (SEM) images of the $NaFePO_4$ nanoclusters which exhibit uniform spherical morphology (100 nm). The elemental mapping images confirm that Na, Fe, P, and O elements are well-distributed over the entire $NaFePO_4$ nanoclusters. The high-resolution Transmission Electron Microscopy (HRTEM) displays image of $NaFePO_4$ nanoclusters which is composed of plenty of ultrafine NFP@C subunits. The carbon content of $NaFePO_4$ nanoclusters is calculated to be 10.3% by Thermogravimetric Analysis (TGA). Cyclic voltammetry (CV) was tested from 0.1 to 2.0 mV s^{-1} to evaluate the Na-migration kinetics of $NaFePO_4$ nanoclusters. The CV curves exhibit two peaks at 2.1 and 3.0 V, causing by the intercalation/deintercalation of Na^+. After first charge, the $NaFePO_4$ electrode delivers a high discharge capacity of 149.2 mA h g^{-1}, corresponding to 96.3% of the theoretical capacity.

The rechargeable sodium ion batteries are the elective material to replace conventional lithium ion batteries for the improvement of next generation devices, considering that iron may been exceptionally reasonable element, and low cost it is the preference for fluid rechargeable batteries have studied by **Karthik et al., (2020) [13]**. The XRD pattern of $NaFePO_4$ exposed sharp intense peaks at 2θ = 32.11, 33.08, and 35.38, corresponding to the miller indices (220), (121) and (002), respectively. The XRD pattern of $NaFePO_4$ confirms that it exhibits an orthorhombic structure with Pnma space group. Raman vibration modes appeared at 1347 and 1587 cm^{-1} are present due to the D and G bands of carbon-based materials. The Fe-O-based Raman modes were located in the 400–700 cm^{-1} wave number region in the $NaFePO_4$ sample. The PO_4 based vibration are positioned at 951, 592 and 422 cm^{-1}. According to FESEM analysis,

$NaFePO_4$ exposed clear hexagonal disk-shaped nanoparticles with average diameter around 70–90 nm and thickness about 20–30 nm, The occurrence of major elements (Na, Fe, P, O and C) in the EDAX spectra gives further proof to formation of $NaFePO_4$. The dielectric properties were analyzed at the frequency range 100Hz to 1MHz. Based on the GCD profile, the discharge capacity of $NaFePO_4$ is estimated about 64, 58, 48, 39, 32, and 23 $mAhg^{-1}$ at a current rate of 0.1, 0.2, 0.5, 1, 2 and 5 C, respectively. $NaFePO_4$ hybrid electrode reached discharge capacity of 90 $mAhg^{-1}$ at corresponding current density of 0.1 C. The $NaFePO_4$ composite maintained 98% of retention after the 100th cycles test. The EIS further hold high electrochemical nature of the $NaFePO_4$.

$Na_{1.7}Fe_3(PO_4)_3$ have been synthesized by **Essehli et al**., **(2020) [14]** via solvothermal method, Sodium vacancies in the crystal structure was characterized by X-Ray Diffraction pattern. . No impurities were detected as confirmed by the **SEM** analyses, which show highly uniform mono-dispersed secondary spherical particles with quite similar sizes. After the first charge and discharge, sodium is intercalated into the vacancies, hence, the nonstoichiometric compositions $Na_{1.7}Fe_3(PO_4)_3$ and $Na_{1.86}Fe_3(PO_4)_3$ are converted into the stoichiometric $Na_2Fe_3(PO_4)_3$. The exchange current density measurement indicates that better electrochemical performance with a practical C-rate could be achieved for $Na_{2-x}Fe_3(PO_4)_3$ as cathode for Na-ion batteries.

$Na_3Fe_2(PO_4)_3$ prepared by **Cao et al., (2020) [15]** through simple spray drying method. The galvanostatic charge-discharge test results indicate that the initial reversible discharge specific capacity of flake-porous $Na_3Fe_2(PO_4)_3$ electrode can reach to 100.8 mAh g^{-1} under a current density of 10 mA g^{-1} (0.1C), and the high rate capability at 500 mA g^{-1} (5 C) is up to 60 mAh g^{-1} after 1100 cycles. As cathode material, the flake-porous $Na_3Fe_2(PO_4)_3$ electrode exhibits excellent electrochemical performance. The cycle stability performance test of $Na_3Fe_2(PO_4)_3$ cathode which indicates initial discharge specific capacity was upto 66.5$mAhg^{-1}$ and maintains 60 $mAhg^{-1}$ after 1100 cycles with the corresponding coulombic efficiency of 100% during all the cycles. The cycle stability performance with in sodium-ion batteries indicates the flake-porous $Na_3Fe_2(PO_4)_3$ exhibits an outstanding electrochemical performance. The excellent cycle stability and low temperature performance prove that the NFP|| $Na_{x+y}C$ sodium-ion full cell is found to be an ideal energy storage device.

Performance of the prepared $NaFePO_4$ cathode material through electrochemical sodiation to $FePO_4$ layer on aluminium substrate is investigated by **Rahmawati et al., in (2020) [16]**. Cyclic voltammetry (CV) studies was conducted to determine the reduction and oxidation potentials of $NaFePO_4$ when cycled in the fabricated batteries. The reduction potentials represent Na^+ intercalation into $FePO_4$ layer, as the batteries being discharged. The oxidation potentials represent Na^+ de-intercalation from $FePO_4$ layer, as the batteries being charged. $NaFePO_4$ cathode delivered a good specific capacity near 154 mAh/g.

Iron-based phosphate $Na_4Fe_3(PO_4)_2(P_2O_7)$ nano-sphere growing on the multi-walled carbon nanotubes have been fabricated by **Cao et al., (2020) [17]** via convenient spray drying method. During the charge/discharge process, the three sodium-ions in M1 and M2 can reversibly insert/extract from the 3D channel structure and the sodium-ion in M3 site can stable the particular structure. The composite cathode exhibits a reversible capacity of 115.7 mA h g^{-1}. A sodium-ion full cell shows a specific energy of 210 Wh.Kg^{-1}.

Nanosized maricite $NaFePO_4$ nanoparticles encapsulated within carbon synthesized have prepared by **Wang et al., (2020) [18]** by a sol-gel method. X-Ray Diffraction (XRD) pattern of nanosized maricite $NaFePO_4$ composite. correspond to space group Pmnb. Nanosized maricite $NaFePO_4$ electrode delivers a high capacity retention, good cyclic stability, and rate capability. No obvious reduction/oxidation reaction peaks were observed within the charge and discharge range, indicative of the capacitive behavior of the electrode nanosized maricite $NaFePO_4$. The discharge specific capacity after five cycles is as high as 140 $mAhg^{-1}$, which is 91% of the theoretical capacity (155 mA h g^{-1}) of $NaFePO_4$.

Sodium iron phosphate [$Na_3Fe_3(PO_4)_4$] successfully synthesized by **Ganesh et al., (2019) [19]** through solution combustion synthesis method. This prepared nanoscale $Na_3Fe_3(PO_4)_4$ compound was found to be electrochemically active with a stepwise voltage profile involving an Fe^{3+}/Fe^{2+} redox activity at 2.43 V vs. Na/Na^+. This limited electrochemical activity can be relatively large diffusion barrier (ca. 0.28 eV) as per Bond valence site energy. Wet chemical synthesis, structure, magnetic and electrochemical properties of a synthesized $Na_3Fe_3(PO_4)_4$, the Na^+ migration and diffusional analysis has been calculated to probe the reason behind electrochemical

limitations. The cell performed with steady capacity (ca. 48 mAh/g) with 98% Coulombic efficiency. Phosphate based compounds are important among the polyanionic insertion materials as they are durable over high temperature and provides more chemical stability along with good electrochemical properties.

The sample olivine $NaFePO_4$ obtained by **Fernandez-Ropero et al., (2019) [20]** via electrochemical delithiation-sodiation method. The X-Ray Diffraction (XRD) pattern have been indexed with Pnma space group. Capacity is obtained with a superior performance of the aqueous cells, especially at high rates, achieving 110 $mAhg^{-1}$ at C/10 and 74 $mAhg^{-1}$ at 2 C. In aqueous electrolyte the polarization was strongly reduced, leading to superior capacity at all tested rates compared to organic electrolyte with a comparable voltage window. Moreover, by fine tuning the voltage window, the capacity retention was notably improved, indicating that this material is a good candidate for aqueous Na-ion batteries. Hence demonstrated that $NaFePO_4$ is a promising candidate for aqueous Na-ion cells.

Nanosized $Na_4Fe_3(PO_4)_2$ (P_2O_7) plates and microporous Na_4Fe_3 $(PO_4)_2(P_2O_7)$ particles have been successfully synthesized by **Chen et al., (2019) [21]** via facile one-step sol–gel method. By the In-situ X-Ray Diffraction (XRD) pattern, confirmed that both the robust reversible crystal framework and the continuous valence change of Fe contributed to the excellent electrochemical performance. Raman spectra were collected to characterize the carbon of both samples. The vibration states of existing functional groups were examined.

The typical vibration modes of both the PO_4 units and the FeO_6 octahedra were also detected in the Fourier transform infrared spectrum. Thermogravimetric (TG) analysis were performed on a Mettler Toledo TGA with a heating rate of 10 °C min^{-1} in air. Cycling stability was obtained without noticeable voltage decay (69.1% capacity retention after 4400 cycles at 20 C) with almost 100% achieved. Specific capacities of the full cell are based on the anodes, the full cell achieves capacity retention of 76.9% at 100 mA g^{-1} over 500 cycles and high Coulombic efficiency near 100%. Nanosized $Na_4Fe_3(PO_4)_2$ (P_2O_7) plates and microporous Na_4Fe_3 $(PO_4)_2(P_2O_7)$ electrode show superior electrochemical performance even in hot climate regions.

Mesoporous Na_2FePO_4F@C composite derived from mesoporous $FePO_4$ through a facile ball-milling combined calcination method by **Zhang et al., (2019) [22]**.

Peak detected in the X-Ray Diffraction (XRD) pattern for $FePO_4$ material, indicates an amorphous characteristic nature of the material. By the Scanning Electron Microscopy (SEM) of the sample Mesoporous Na_2FePO_4F@C with little carbon content shows the primary particle sizes of 100 nm. Carbon coating layer of about 4 nm can be seen clearly in the high-resolution transmission electron microscope (HR-TEM). Moreover, uniform distribution of Na, Fe, P, O, and F in Na_2FePO_4F@C particles was measured by energy-dispersive X-ray (EDX) mapping. Cyclic Voltammetry (CV) curves of the Mesoporous Na_2FePO_4F@C electrodes at a scanning rate of 0.1 mV s^{-1} in the potential range of 2–4 V. Mesoporous Na_2FePO_4F@C electrode can deliver a capacity of 110 mAh g^{-1}, corresponding to almost 96% capacity retention compared to its initial capacity.

Prepared $NaFePO_4$ cathodes containing both amorphous and maricite phase which exhibits much improved sodium storage performance have been studied by **Xiong et al., (2018) [23]**. X-Ray Diffraction (XRD) pattern of a prepared maricite sample gives the pure single phase, that is the maricite-type $NaFePO_4$ phase. By the Raman spectra the existence of carbon phase by the two characteristic bands in the range of 1200-1700 cm^{-1} is verified.

The electrochemical performance was characterized by measuring the galvanostatic charge/discharge cycling behaviour in the potential range of 1.5-4.5 V. An initial capacity of 115 $mAhg^{-1}$ at 1C and an excellent cycling stability of capacity retention 91.3% after 800 cycles. This cycling is longer than that of the most reported maricite based $NaFePO_4$ based materials. The derived amorphous $NaFePO_4$ exhibits better electrochemical activity due to the enhancement of Na mobility. $NaFePO_4$ attracts much attention owing to its high theoretical capacity (155 $mAhg^{-1}$) low cost high structural stability and non-toxicity.

Prepared Sodium ion pyrophosphate ($NaFeP_2O_7$ and $Na_{1.5}6Fe_{1.22}P_2O_7$) is derived by **Kosova et al., (2017) [24]** through solid state synthesis method mechanochemically and the material was characterized by XRD, FTIR, SEM, EDX, and galvanostatic cycling. The structure of the prepared pyrophosphates, refined in a triclinic symmetry differing by the amount of occupancy of Fe and Na sites and also the disorders in the structure. The structural characterization of synthesized product was analysed by X-ray powder diffraction (XRD). According to the SEM analysis the

prepared sample consists of mixture of fine particles with an average particle size of about 300-500 nm and larger micron sized particles originated as a result of agglomeration of primary particles. The crystallization temperature of the final products $Na_{2-x}Fe_{1+x/2}P_2O_7$ (x=0; 0.44) was determined by Thermogravimetry and differential thermal analysis (TG/DTA) by heating the mixtures under an Argon atmosphere. The charge-discharge profiles of the first and the fifth cycles of the prepared $Na_2FeP_2O_7$ in a Na-cell at C/20 rate within the 2.0-4.3 V range. The sample contained a considerable amount of the Fe^{3+} ions according to Mossbauer spectroscopy. Initial discharge capacity of $Na_2FeP_2O_7$ is 89 $mAhg^{-1}$, corresponding to 92% of the theoretical capacity. Hence pyrophosphate shows good electrochemical performance with better capacity retention on cycling

Iron-rich sodium iron phosphate have been synthesized by **Lu et al., (2017) [25]** via solid state reaction method. The XRD pattern of $Fe_{1.2}PO_4$ only shows little change involving small peak shift to higher angles and change in relative peak intensity, suggesting that volume shrinkage is small during Na deintercalation. During the electrochemical cycling at the current rate of C/20, and a reversible capacity of 85$mAhg^{-1}$ was obtained approaching the theoretical capacity of 91.4 $mAhg^{-1}$. Iron-rich sodium iron phosphate is found to be electrochemically active, delivering the reversible capacity of 85 $mAhg^{-1}$. This new iron based poly anionic compounds such as $Na_2FeP_2O_7$ will reduce the cost of cathode materials. Hence the sodium iron-rich orthophosphate compound as potential cathode for sodium ion batteries. Maricite $NaFePO_4$ phase became negligible and the new phase was determined as $Na_{0.6}Fe_{1.2}PO_4$. Phosphate compounds have been investigated as cathode material for sodium ion batteries. This reveals that the importance of off-stoichiometric compounds as cathode materials.

Maricite-$NaFePO_4$ have fabricated by **Kapaev et al., (2017) [26]** by solid state method. X-ray diffraction (XRD) data showed maricite-$NaFePO_4$ (m-NFP) samples contained a single phase with maricite structure, the composition of the synthesized samples corresponded to $NaFePO_4$. Raman spectra of obtained samples exhibited two bands at 1600 and 1350 cm^{-1}, usually referred to as the G-band D-band, respectively. The G-bands are strong and narrow, indicating a high content of sp^2-carbon in the coating. The charge–discharge rate (0.1 C). There is a dramatic increase in the $NaFePO_4$ capacity up to 150 mAh g^{-1}. Composite $NaFePO_4$ exhibit high capacities after an

increase in charge–discharge rate up to 150 mA g^{-1}. The capacity increase for the obtained materials could be caused by the partial $NaFePO_4$ phase amorphization. This denotes good prospects for $NaFePO_4$ application in the Sodium ion batteries. Initial particle size of 20–30 nm and the efficient carbon coating were insufficient to reach good electrochemical performance. Capacity increase can be achieved using the mechanochemical activation of the material.

Uniform carbon-coated $Na_{3.32}Fe_{2.3}4(P_2O_4)_2/C$ composite represent a promising alternative for sodium-ion batteries is investigated by **Chen et al., (2017) [27]**. The XRD pattern shows the triclinic P−1 space group. Raman spectra indicates the presence of the carbon-coating layer of $Na_{3.32}Fe_{2.3}4(P_2O_4)_2/C$ (NFP/C) with obvious D and G bands located at 1350 and 1600 cm^{-1}, and almost no specific peaks of $Na_{3.32}Fe_{2.34}(P_2O_7)_2$ can be found.

It delivers capacity of about 100 $mAhg^{-1}$ at 0.1C, with the capacity retention of 92.3% at 0.5C after 300 cycles. There is a small volume change, nearly 100% first-cycle coulombic efficiency. Almost, 100% first-cycle coulombic efficiency was achieved, which is quite critical for sodium ion batteries. There is a tiny volume change approximately 2.19% during electrochemical cycling which is also a reason for the superior cyclability. Hence low cost, high stability pyrophosphate composite $Na_{3,32}Fe_{2.34}(P_2O_4)/C$ material is the most promising candidates for extensive application in large scale Na rechargeable batteries.

Reversible nature of Fe^{3+}/Fe^{4+} redox couple and the electrochemical performance of $Na_3Fe_2(PO_4)_3$ cathodes is reported by **Rajagopalan et al., (2017) [28]**. The phase purity of synthesized NASICON-type $Na_3Fe_2(PO_4)_3$ was confirmed by the powder XRD. The Raman analysis of the $Na_3Fe_2(PO_4)_3$ showed two high intensity peaks at 1353 and 1592 cm^{-1}, corresponding to the D and G bands of carbon, respectively. The scanning electron microscopy (SEM) image of the pristine $Na_3Fe_2(PO_4)_3$ powder, exhibiting irregularly agglomerated particles. The Transmission electron microscopy (TEM) image showed that the $Na_3Fe_2(PO_4)_3$ is wrapped by carbon. The Cyclic Voltammetry (CV) analyses revealed the formation of Fe^{4+} oxidation state in the charged cell. $Na_3Fe_2(PO_4)_3$ exhibited a discharge specific capacity of 109 $mAhg^{-1}$ and cycling stability with 96% capacity retention after 200 cycles. $Na_3Fe_2(PO_4)_3$ is

found to be an appropriate active component that gives good electrochemical performance of a full working cell.

Nanocomposite $NaFePO_4$ fabricated by **Priyanka et al., (2017) [29]** sol-gel and solid state method and its structure was analyzed. The XRD patterns of the as prepared samples $NaFePO_4$ by solid state and sol-gel method showed olivine structure. The sample obtained by sol-gel method was found to be more crystalline than solid state reaction. The FTIR spectrum was analyzed for the presence of functional groups. The analysis carried out in the area of PO_4 group oscillations. From the SEM analysis, $NaFePO_4$ sample was prepared by sol-gel method and its particle size is found to be in the range of 100 – 200nm, and the $NaFePO_4$ sample was prepared by solid state method appears to be in cluster form, caused by the direct condensation polymerization of phosphate groups. The results revealed that as-prepared $NaFePO_4$ nano composite prepared by sol-gel method serves as promising cathode material for sodium ion batteries.

Submicron sized $NaFePO_4$ is in-situ by an electrochemical alkali metal cation displacement technique is successfully synthesized by **Heubner et al., (2017) [30]**. X-Ray Diffraction (XRD) analyses of the intermediate phase, $Na_{2/3}FePO_4$, indicates the existence of a superstructure that could result from Na/vacancies and the formation of $NaFePO_4$ are verified by X-ray diffraction.

Therefore, the electrodes are charged and discharged at a rate of C/20 to different states of sodiation starting from the fully sodiated or desodiated state $NaFePO_4$ / $FePO_4$, the equilibrium potential was measured until stable conditions have been achieved. Due to the asymmetric phase transition behavior, the properties of the solid electrolyte interface may depend on whether the electrode is charged or discharged, resulting in a path dependence of the reaction kinetics. Electrochemical impedance spectroscopy (EIS) are performed to investigate the sodium insertion and extraction 350 kinetics. The exchange current density and the apparent sodium diffusion coefficient significantly depend on the sodium concentration in the active material. Submicron sized $NaFePO_4$ having 80 % of the theoretical capacity (154 mAh g^{-1}).

Sodiated iron phosphate synthesized by solid state method and its electrochemical performance is reported by **Liu et al., (2016) [31]**. The results of XRD pattern indicate that, the trigonal $FePO_4$ formed an electrochemically inactive phase, In

addition, the size of the trigonal $FePO_4$ nanoparticles became much larger, which can slow the active material/electrolyte interface reaction by decreasing the specific surface area. . The Cyclic voltammatery (CV) is unable to measure the D(E) or D(c) dependence or may even fail to detect its existence. This is a "weak point" for the CV technique in measuring the diffusion coefficient of intercalated ions. The outstanding electrochemical performance of amorphous $FePO_4$ was attributed to the amorphous and triphylite $NaFePO_4$ with high electrochemical activity. Those findings indicate that amorphous $FePO_4$ can be transformed into active $NaFePO_4$, which may have great potential as an electrode material for sodium-ion batteries. The low cost, easy synthesis, environmentally friendly properties, and high theoretical capacity (178 mA h g^{-1}) of $FePO_4$ have recently made it the focus of research as a cathode material in rechargeable batteries.

Na_2O-FeO-P_2O_5 glasses for sodium ion batteries prepared by **Nakata et al., (2016) [32]** and studied the glass formation tendency, crystallization behavior, electrical conductivity as well as charge and discharge properties. By the XRD pattern values of the crystallization peak (Tp) was increased. Therefore the primary crystallized phase was confirmed as $NaPO_3$ in 20FeO-80$NaPO_3$ by means of XRD. Raman bands at 740 cm^{-1} which is assigned as P-O-P symmetric stretching modes are also appeared. All samples have Q1 species that means polymerized phosphates are existing in glass matrix. From the DTA (Differential Thermal Analysis) patterns for the as-quenched sample, the endothermic peaks due to the glass transition and exothermic peaks due to the crystallization are clearly observed. Charge and discharge profiles for Na anode exhibits high reversible discharge capacity as 115 mAh/g at 0.1 °C rate. Triclinic P1 $Na_2FeP_2O_7$ exhibits 3.0 V, 97 mAh/g with good cyclic performance. $Na_2FeP_2O_7$ is also available in aqueous based sodium ion batteries which implies good chemical stability. It is known that glass have large free volume and flexible open structure, hence superior alkali ion conduction exhibits in glass-ceramic derived solid state electrolytes for lithium ion batteries and sodium ion batteries as well.

Performance of sodium iron phosphate ($Na_3Fe_2(PO_4)_3$ as cathode material by solid state reaction method is investigated by **Liu et al., (2016) [33]**. The X-ray Diffraction (XRD) pattern indicates the structure of prepared $Na_3Fe_2(PO_4)_3$ is monoclinic in the space group C2/c.

High-Resolution Transmission Electron Microscopy (HR-TEM) images exhibited no lattice fringe, of the precursor sample. The initial discharge/charge specific capacities are about 61 mAh g^{-1} with very flat voltage plateaus located at about 2.5 V, in good agreement with the results of cyclic voltammetry test, and the sodium ion diffusion is calculated using the cyclic voltammetry test. The initial coulombic efficiency was up to 95% and remained close to 100% during all the cycles. The reversible capacity of $Na_3Fe_2(PO_4)_3$ was 61 $mAhg^{-1}$ and was maintained at 57 $mAhg^{-1}$ after 5oo cycles without obvious fading of the capacity, Hence there is an excellent rate capacity and cyclic stability of $Na_3Fe_2(PO_4)_3$ cathode material clearly proved that $Na_3Fe_2(PO_4)_3$ is a potential cathode material for sodium ion battery (SIB). $Na_3Fe_2(PO_4)_3$ compound showed electrochemical activity, and good specific capacity even though the current density is low, the low cost and environmental friendliness of $Na_3Fe_2(PO_4)_3$ might have extensive application prospects in energy storage system.

Mixed polyanionic $Na_4Fe_3(PO_4)_2(P_2O_7)$/C nanocomposite is synthesized by **Wu et al., (2016) [34]** through the sol-gel method. In-situ X-Ray Diffraction (XRD) pattern demonstrate that the sodium insertion/extraction process in $Na_4Fe_3(PO_4)_2(P_2O_7)$/C is an imperfect solid-solution reaction with an obvious local lattice distortion instead of an ideal solid-solution reaction.

The scanning electron microscopy (SEM) image reveals that most of the particle sizes are in the range of 100 to 150 nm. The long-term cycling stability of $Na_4Fe_3(PO_4)_2(P_2O_7)$/C is demonstrated at a rate of 0.5C, retaining 89% of the initial discharge capacity after 300 cycles. polyanionic $Na_4Fe_3(PO_4)_2(P_2O_7)$/C can deliver an initial capacity of 110 mAh g^{-1} , hence it is a promising cathode material for sodium ion batteries, which is expected to be applied in large-scale energy storage.

Olivine $NaFePO_4$/C microsphere cathode have been synthesized **Fang et al., (2015) [35]** by a facile aqueous electrochemical displacement method. To confirm the presence of the intermediate phase at high discharge rate, ex-situ X-ray diffraction (XRD) was employed to characterize the phase transformation during the whole Na ion intercalation process in the $FePO_4$/C electrode.

Scanning Electron Microscopy (SEM) and Transmission Electron Microscopy (TEM) observation further revealed that the obtained $NaFePO_4$/C composites remained microspherical structure. The corresponding elemental mappings of Na, Fe, P, and O,

are exhibiting a uniform element distribution in the microsphere. The element dispersive spectroscopy (EDS) spectrum analysis shows that the Na/Fe/P/O ratio is nearly 1:1:1:4, indicating that the microsphere is $NaFePO_4$. Cyclic voltammetry (CV) and constant current charge discharge demonstrates the direct electrochemical conversion from $LiFePO_4$/C to $NaFePO_4$/C in aqueous solutions, respectively. Charge discharge profiles of Olivine $NaFePO_4$/C microsphere cathode, exhibiting excellent Na ion intercalation/deintercalation reversibility. The $NaFePO_4$/C cathode displays a high discharge capacity of 111 mAh g^{-1} along with 90% capacity retention over 240 cycles at 0.1 C and high rate capacity. The excellent electrochemical performance demonstrates that the electrochemical displacement method offers an inexpensive, effective and promising approach to prepare $NaFePO_4$/C materials for Na-based energy storage applications.

Na_2O-Fe_2O_3-P_2O_5 fabricated by **Honma et al., (2014) [36]** via conventional melt-quenching method. The glass ceramics consists of crystals with a triclinic P1 phase by controlling heat treatment temperature, time, and atmosphere. XRD patterns for the heat-treated samples with x = 0, indicates that the main crystalline phase is triclinic P1 phase. The formation of $Na_4P_2O_7$ phase is also detected as byproduct, and the intensity of its diffraction peaks increases with increasing heat treatment temperature. Through the SEM (Scanning electron microscope) grains with a particle size of several micrometers are observed. In particular, the needle-shaped crystals are present at the surface of the sample. The amount of carbon content was identified by thermogravimetric analysis (TG-DTA). The glass-ceramics with showed a reversible discharge capacity of 83 mAh/g hence $Na_2FeP_2O_7$ exhibits good electrochemical performance.

Sodium iron phosphate with a Maricite structure were synthesized by **Prosini et al., (2014) [37]** by hydrothermal method and solid-state synthesis. Phase identification was performed by (X-Ray Diffraction) XRD analysis. Scanning electron microscope (SEM) technique may be related to the fact that the material is not uniform in size and can present an internal porosity.

The presence of various size fractions and intercommunication networks within the particles can give rise to a specific surface area greater than that apparent. Thermogravimetry Analysis (TGA) curves shows the same thermal profile and the

same increase in weight between 320 °C and 520 °C. Electrochemically prepared $NaFePO_4$ could deliver a specific capacity of 125 mAh g^{-1} over 50 charge–discharge at room temperature and under a very low charge–discharge rate (C/20). Therefore, it is likely that proceeding toward this direction will be possible to further improve the performance of the material in order to achieve a sodium-ion battery with a cost/performance ratio competitive with lithium battery systems.

Amorphous carbon coated $Na_7Fe_7(PO_4)_6F_3$, by combining hydrothermal and solid state reaction methods is synthesized by **Ramireddy et al., (2014) [38]**. Using high resolution synchrotron X-Ray Diffraction (XRD) data, impurities were found to differ between the pristine and carbon-coated $Na_7Fe_7(PO_4)_6F_3$ electrodes which may also contribute to the noted differences in performance at high current rates. Scanning Electron Microscope (SEM) images of pristine $Na_7Fe_7(PO_4)_6F3$ and $Na_7Fe_7(PO_4)_6F_3$/C composite show that both samples consist of numerous clusters. Transmission Electron Microscope (TEM) bright-field imaging of the pristine $Na_7Fe_7(PO_4)_6F_3$ sample exhibits a dense agglomerate cluster. The potential plateaus observed in the charge/discharge curves are consistent with the CV results. $Na_7Fe_7(PO_4)_6F_3$/C delivers a reversible capacity of 65 mA h g^{-1} at 100 mA g^{-1}. Therefore, the carbon-coated $Na_7Fe_7(PO_4)_6F_3$ composite presents feasible sodium intercalation/de-intercalation capacity, offering possibilities for developing a low cost, high performance sodium-ion battery positive electrode.

Sodium iron pyrophosphate using the solid state reaction method which is reported as the safe cathode material with high thermal stability by **Barpanda et al., (2013) [39]**. Cathode material pyrophosphate $Na_2FeP_2O_7$ adopts a triclinic three-dimensional framework. XRD study reveals a steady and reversible shift in peak positions during electrochemical cycling of the $Na_2FeP_2O_7$ cathode, indicating the possibility of single-phase redox activity throughout the potential range.

Thermogravimetric (TG) curve shows no weight change. The combination of an exothermic peak with no weight change points at a possible phase transition of β-$NaFeP_2O_7$ is observed. Galvanostatic charge− discharge profiles of $Na_2FeP_2O_7$ at a rate of C/10 for the first 30 cycles shows the chemical desodiation of insertion compound which lead to the formation of new polymorph. High operational stability is obtained in pyrophosphate $(P_2O_7)^{4-}$ anion, which gives better safety than the other phosphate

based cathode. The pyrophosphate cathode tend to deliver higher operational safety although the net capacity is lower owing to the weight penalty. $Na_2FeP_2O_7$ have a moderate capacity of 90 mAh/g at 3 V vs Na/Na+, with excellent safety and hence it is used in large-scale batteries for grid power storage.

$NaFePO_4$ Maricite phase prepared by **Moreau et al., (2010) [40]** under hydrothermal conditions and $NaFePO_4$ olivine structure along with that of an intermediate is produced. XRD pattern shows all the reflections of the powder pattern which can be indexed assuming space group of C2/c. Hence the structural type of $Na_3Fe(PO_4)_2$ is isotypic with ferroelectric phase. This strucure type is isotypic with the ferroelastic phase of $NaFe(MoO_4)_2$ in which Na(2) site is vacant. As a consequence of this, ferroelastic properties may be expected. The $Na_{0.7}FePO_4$ was obtained with high purity of equilibrating the sample at 2.95V versus Na/Na^+. The sodium site occupancy was refined as 1.003(12), confirming the fuel intercalation. The $NaFePO_4$ cell parameters are slightly larger than the lithium equivalent. Two new Na_xFePO_4 phases were synthesized electrochemically and their olivine-based structures are reported, it has good cycling properties with noticeable difference in $NaFePO_4$ hence sodium battery technologies based on olivine iron phosphates.

Synthesized $NaFePO_4(PO_4)_3$ electrode and k-doped into the host material which is an effective way to increase the ionic conductivity performance and its analyzed by **Cao et al., (2010) [41]**. The XRD pattern of K-doped $NaFe(PO_4)_3$ powders can be refined to the monoclinic NASICON structure in the space group of C2/c. Cyclic voltammetry(CV) results indicate that all the electrode materials have one pair of peaks which located at 2.47/2.65 V attributing to the Fe^{3+}/Fe^{2+} redox couple. K-doping method is a significant way to improve the cycle stability and rate capability performance of cathode material in SIBs. According to electrochemical measurement results, the K-doped method will increase the Na^+ diffusion coefficient and improve the electrochemical performance for SIBs. When compared to the undoped $Na_3Fe_2(PO_4)_3$ sample $K_{0.2}$ NFP electrode shows a 101.2mAh g^{-1} which reaches upto 97% of theoretical capacity. Hence high cyclic stability and excellent performance is obtained.

CHAPTER III

MATERIALS AND METHODS

3.1 INTRODUCTION

This chapter deals with the experimental techniques used in the preparation and characterization of $NaFe_{0.98}Zr_{0.02}PO_4$. Sol-gel method is used for the preparation of the chosen material. The characterization of the prepared material is analysed by the following experimental techniques, such as

- X-ray Diffraction (XRD)
- Field Emission Scanning Electron Microscope (FESEM)
- Thermogravimetric-Differential thermal analysis (TG-DTA)
- Raman Spectroscopy (RS)
- Cyclic Voltammetry (CV)

3.2 Preparation of $NaFePO_4$ and $NaFe_{0.98}Zr_{0.02}PO_4$

$NaFePO_4$ was synthesized via the sol-gel method. Initially, appropriate amounts of ferrous oxalate dihydrate and sodium nitrate are dissolved in 60 ml solution of diluted nitric acid [Sol A]. Sol A is stirred until the salts get completely dissolved. 10 ml of Ammonium dihydrogen phosphate [Sol B] is stirred until it gets dissolved in water. A 1.2668g of citric acid monohydrate salt is dissolved in 20 ml of [Sol C] distilled water under magnetic stirring. Sol B and C were added to sol A and it is kept at 150°C under magnetic stirring until a gel is formed. The obtained gel is kept in water bath at 150°C for 3 hours and a dry product is obtained after the removal of excess ammonia from the sample. And it is finely ground and calcined at 700°C for 2 hours. The same procedure is repeated for the Zr doped sample by the addition of 0.02g of Zirconyl (IV) nitrate hydrate ($ZrN_2O_7.H_2O$) with Sol A. These samples are taken for further characterizations.

3.2.1 Electrochemical testing:

Electrochemical studies are carried out using **$NaFePO_4$** and **$NaFe_{0.98}Zr_{0.02}PO_4$** as a working electrode and it is composed by the mixture of active material, polyvinyl fluoride (PVDF) as binder and carbon black as additive in the ratio of 85:10:5. Then the mixture is mixed with N-methyl pyrrolidinone (NMP) solvent to form a slurry. Then the slurry is coated on copper foil, and dried at 80°C to ensure the complete evaporation of NMP.The prepared electrode is tested

in two alkaline electrolytes viz., 1M sodium hydroxide (NaOH) pellets dissolved in distilled water. Then the prepared electrode is tested using three electrode system with **$NaFePO_4$** and **$NaFe_{0.98}Zr_{0.02}PO_4$** as a working electrode. The Ag/AgCl electrode is used as the reference electrode and platinum as the counter electrode.

3.3. CHARACTERIZATION TECHNIQUES:

This chapter describes the principle, working and experimental set ups utilized for various measurements toward the characterization of the synthesized sodium iron phosphate. The techniques adopted to characterize the nanoparticles are: X - ray diffraction (XRD), Field Emission Scanning Electron Microscopy (SEM), Thermogravimetric-Differential thermal analysis (TG-DTA), Raman Spectroscopy, and Cyclic voltammetry (CV).

3.3.1 POWDER X-RAY DIFFRACTION (XRD)

- X-ray powder diffraction (XRD) has been the most used technique to confirm that the desired phase was obtained after each synthesis.
- XRD is a non-destructive technique, essential for the study of materials, and especially, for structural characterization
- XRD is used to identify the atomic and molecular structure of a crystal **[42].**

3.3.1 (a) Principle of XRD

- This technique is based on the irradiation with an X-ray beam, with a determined intensity (I) and a wavelength (λ) with a similar order of magnitude than the interatomic distance between the atoms of the crystal.
- X-rays diffract by atoms that are dispersed in a particular direction that depend on the crystal structure of the material.
- Although these waves cancel one another out in most directions through destructive interference, some of them add constructively in a few specific directions, determined by Bragg's law,

$$n\lambda = 2d \sin\theta \text{------(1)}$$

where n is an integer number which refers to the diffraction order, λ is the wavelength of the incident x-ray beam, d is the spacing between the planes in the atomic lattice and θ is the angle between the incident ray and the scattering planes. **[43]**

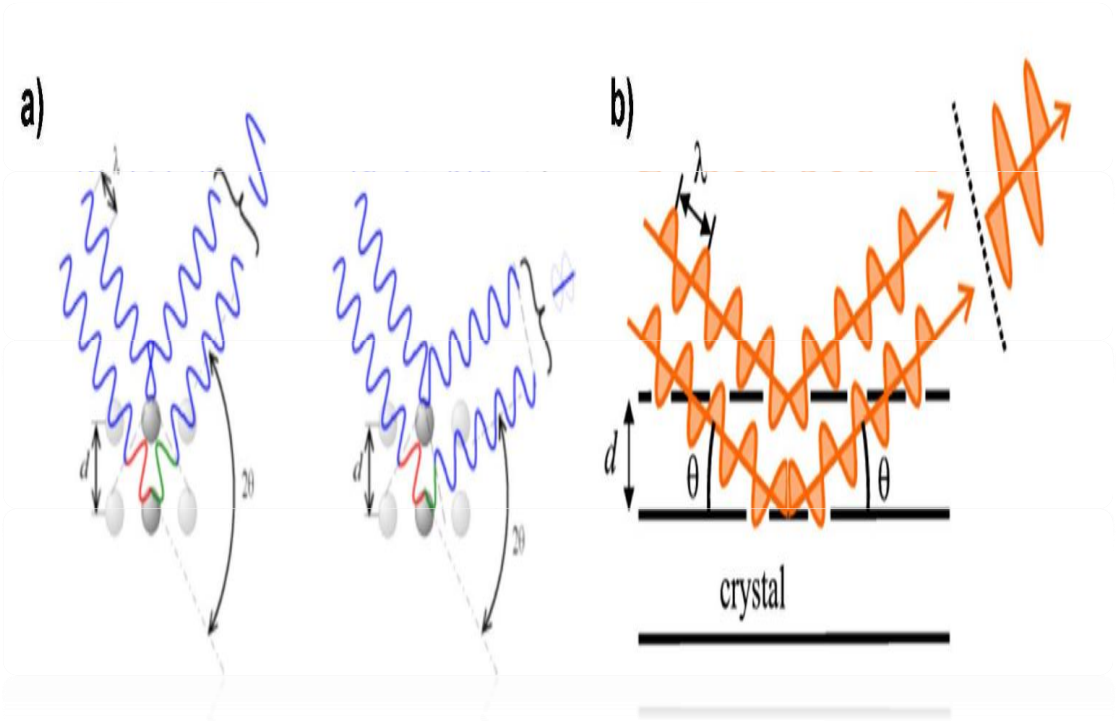

Figure: 3.1. (a) Constructive interference (left) and destructive interference (right) of two-wave fronts and (b) Schematic description of the diffraction of lattice planes according to W.L. Bragg.

3.3.1 (b) Instrumentation of XRD

The three programs that are essential for data collection and analysis are,

1. Data Collector (instrument control and data collection)
2. High Score Plus (data analysis)
3. Data Viewer (data visualization and analysis) [44].

Figure: 3.2 PANalytical X-Pert pro instrument.

- X-ray diffraction data of the prepared samples were detected by PANalytical X-Pert pro instrumentation.
- The instrument can be coupled to many attachments but by default configured in the reflection mode.
- The data collection is controlled by PANalytical data collector software and data analysis performed using PANalytical highscore plus with PDF database.
- The computer that controls the instrument has dual monitors and allows simultaneous data collection of new sample and data analysis of collected samples.

3.3.1 (c) Applications

The main use of XRD is the identification of unknown crystalline materials.

These can be inorganic compounds or minerals, for example.

- Geology
- Engineering
- Biology
- Material science
- Environmental science

- Battery Research
- Thin-film coatings
- Electronics
- Pharmaceuticals

X-Ray Diffraction for defining thin film samples, by using the following techniques:

- Measuring the lattice mismatch between film and substrate to define stresses and strains
- Analysing rocking curves to determine dislocation density and film quality
- Measuring superlattices in epitaxial structures that are multi-layered
- Analysing glancing incidence X-ray reflectivity measurements to determine the thickness, density and roughness of films.

3.3.1. (d): Advantages and Disadvantages in X-Ray Diffraction

The main advantages of x-ray diffraction are:

- It is a rapid and powerful technique for identifying unknown minerals and materials
- It only requires preparation of a minimal sample for analysis
- Interpreting the resulting data is relatively straightforward
- XRD measurement instruments are widely available

Limitations

- Homogeneous and single phase material is best for identification if unknown
- Must have access to a standard reference file of inorganic compounds (d-spacings, hkls).
- Requires tenths of a gram of material which must be ground into a powder
- For mixed materials, detection limit is ~ 2% of sample. For unit cell determinations, indexing of patterns for non-isometric crystal systems is complicated.
- Peak overlay may occur and worsens for high angle 'reflections' **[45].**

3.3.2. FIELD EMISSION SCANNING ELECTRON MICROSCOPY (FESEM)

A Field Emission Scanning Electron Microscopy (FESEM) is used to visualize very small topographic details on the surface or entire or fractioned objects.

Researchers in biology, chemistry and physics apply this technique to observe structures that may be as small as 1 nanometer (= billion of a millimeter).

Figure: 3.3 Field Emission Scanning Electron Microscope

3.3.2 (a) Principle

FESEM is the abbreviation of Field Emission Scanning Electron Microscope.

A FESEM is microscope that works with electrons (particles with a negative charge) instead of light. These electrons are liberated by a field emission source.

The object is scanned by electrons according to a zig-zag pattern **[46].**

3.3.2 (b) Instrumentation

1. A cryo-FESEM looks like a cylindrical column (1) that is mounted on a desk.
2. The column hosts the electron beam. Knobs for the regulation of the electron beam can be found at various levels on the column.
3. There are also tubes present to maintain the vacuum and the temperature in the instrument and the cryo-unit. The microscope is operated from the steering panel .

4. A close copy of this panel has been used for the simulations.

5. The cryo-unit with a binocular is located at left of the column. When conventional (not cryo) microscopy is applied the exchange chamber in front, below the columns is used to introduce the object into the high vacuum area.

6. The object can be observed on the large screen while it is scanned.

7. The small screen serves to watch the object chamber. The computer for image archiving and processing is located right.

8. The cupboards below the desk contain electronics .

9. On the background the sound of the pumps that maintain the vacuum in the column can be heared as well as the boiling nitrogen for the freeze-unit and the cooling of the column

3.3.2 (c) Working

- Electrons are liberated from a field emission source and accelerated in a high electrical field gradient.
- Within the high vacuum column these so-called primary electrons are focussed and deflected by electronic lenses to produce a narrow scan beam that bombards the object.
- As a result secondary electrons are emitted from each spot on the object. The angle and velocity of these secondary electrons relates to the surface structure of the object.
- A detector catches the secondary electrons and produces an electronic signal.
- This signal is amplified and transformed to a video scan-image that can be seen on a monitor or to a digital image that can be saved and processed further.

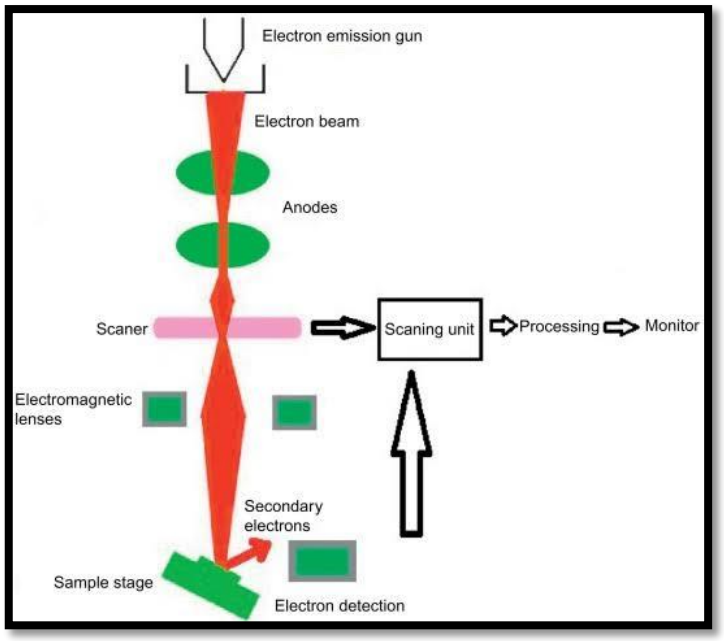

Figure 3.4 Working principle of field emission scanning electron microscope

3.3.2 (d) Applications of FESEM

- Microscopic feature measurements
- Corrosion evaluations
- Striation measurements for high-cycle fatigue fractures
- Coating evaluations
- Characterization of very fine specimen features
- Fracture characterization for polymers and very small components
- Surface contamination analysis
- Small component material analysis
- Laser and resistance weld evaluation
- Printed and integrated circuit analysis
- Microstructure studies **[47].**

3.3.2 (e) Advantages of FESEM

- FESEM has the ability to examine minor area contamination spots at electron accelerating voltages well-matched with EDS.
- In field emission TEM, penetration can be reduced with the aid of low-kinetic-energy electrons that probe nearer to the immediate material surface. Moreover, high-quality and low-voltage images with slight electrical charging of samples can been obtained

using FESEM. One of the striking features of FESEM is that insulating materials need not be coated with conducting materials **[48].**

3.3.2 (f) Disadvantages of FESEM

This type of microscope is a large, cumbersome, expensive piece of equipment, extremely sensitive to vibration and external magnetic fields. It needs to be kept in an area large enough to contain the microscope as well as protect and avoid any unintended influence on the electrons

3.3.3 Thermogravimetric-Differential thermal analysis (TG-DTA)

3.3.3 (a) Thermogravimetric Analysis

The analysis of the change in the mass of a sample on heating is known as Thermogravimetric analysis (TG). TG measures mass changes in a material as a function of temperature (or time) under a controlled atmosphere **[49].**

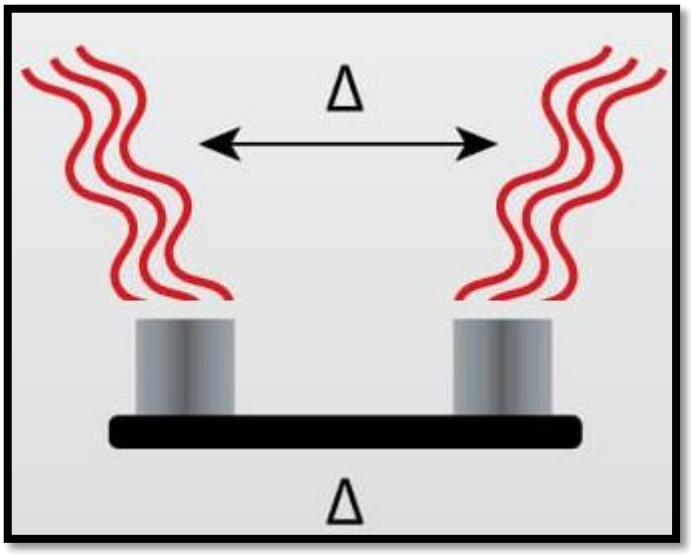

Figure 3.5: TG-DTA Measuring thermal stability.

Principle of Thermogravimetric Analysis:

- A **Thermogravimetric Analysis (**TGA) analysis is performed by **gradually raising the temperature of a sample in a furnace as its weight is measured on an analytical balance that remains outside of the furnace**. In TGA, mass loss is observed if a thermal event involves loss of a volatile component.

- Its principal uses include measurement of a material's thermal stability and composition.
- TG is most useful for dehydration, decomposition, desorption, and oxidation processes.

3.3.3 (b) Differential thermal analysis

- The most widely used thermal method of analysis is Differential thermal analysis (DTA).
- In DTA, the temperature of a sample is compared with that of an inert reference material during a programmed change of temperature.
- The temperature should be the same until thermal event occurs, such as melting, decomposition or change in the crystal structure.

Principle of Differential thermal analysis:

- A technique in which the difference in temperature between the sample and a reference material is monitored against time or temperature while the temperature of the sample, in a specified atmosphere, is programmed **[50].**

TG-DTA modes can be used to determine the following:-

- Melting points
- Glass transition temperatures
- Crystallinity
- Moisture/ volatile content
- Thermal and oxidative stability
- Purity
- Transformation temperatures **[51]**

Table: 3.1 Thermal analysis technique

Techniques	Quality measured
Thermogravimetric analysis (TGA)	Weight change
Differential thermal analysis (DTA)	Temperatures of transitions and reactions

3.3.3 (c) Instrumentation and working of Thermogravimetric Analysis

- The Thermogravimetric analysis instrument usually consists of a high-precision balance and sample pan.
- The pan holds the sample material and is located in a furnace or oven that is heated or cooled during the experiment.
- A thermocouple is used to accurately control and measure the temperature within the oven.
- The mass of the sample is constantly monitored during the analysis. An inert or reactive gas may be used to purge and control the environment.
- The analysis is performed by gradually raising the temperature and plotting the substances weight against temperature.
- A computer is utilized to control the instrument and to process the output curves **[52].**

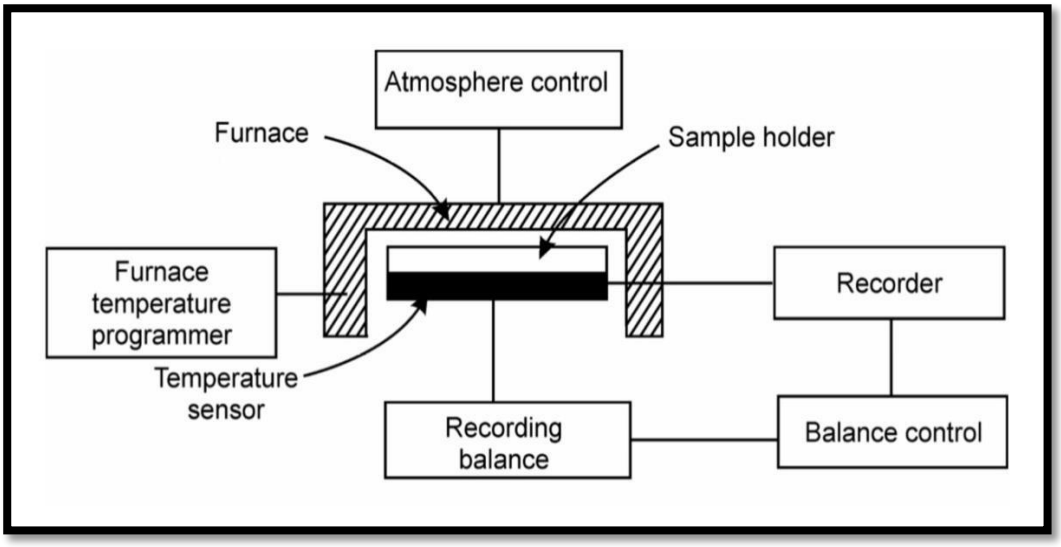

Figure 3.6 Instrumentation of Thermogravimetric analysis.

3.3.3 (d) Instrumentation and working of Differential Thermal Analysis (DTA)

Differential Thermal Analysis (DTA) data are accurate of all thermal techniques, because the thermocouple is inserted into the sample and only the temperature of transition and not the amount of heat can be measured from a DTA curve.

The various component of a DTA apparatus are as following:

- **Furnace**- this is device for heating the sample.

- **Sample holder**- this is used to contain the sample as well as the reference material.
- **DC amplifier**- generally a low level DC amplifier is employed.
- **Differential Temperature Detector**- the function of this detector is to measure differential temperature.
- **Furnace Temperature Programme**- the main function of this is to increase the temperature of the furnace at a steady rate.
- **Recorder**- this is to record the DTA curve.
- **Control Equipment**- its function is to maintain a suitable atmosphere in the furnace & sample holder.

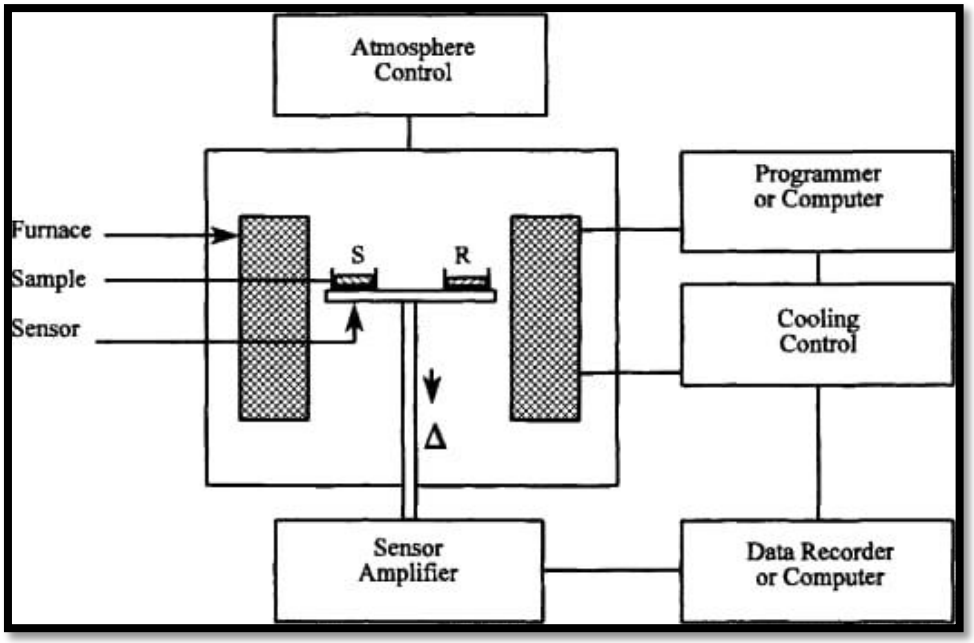

Figure. 3.7 Instrumentation of Differential Thermal Analysis.

- Commercial differential thermal-analyzer system.
- The thermocouple on the right controls the rate at which the furnace must be heated in order to provide a linear temperature increase.
- Any current due to a temperature difference between the two is amplified and used to determine the position of a recorder pen.

- With the switch in position, the sample thermocouple is connected not only to the reference thermocouple but also to a reference junction, which may be at room or ice-bath temperature.
- The output of this circuit provides a measure of the sample temperature at any instant.
- Generally, the sample and reference chamber in a differential thermal apparatus is designed to permit the circulation of inert or reactive gases.
- Some systems also have the capability for operation at high or low pressures.

3.3.3 (e) Applications of Thermogravimetric-Differential thermal Analysis

Applications of Thermogravimetric Analysis

Study of polymeric materials including,

- Thermoplastics
- Thermosets
- Elastomers
- Composites
- Plastic films
- Fibres
- Coatings
- Paints
- Fuels.

Applications of Differential Thermal Analysis (DTA)

The various important applications of DTA are:

- Rapid identification of the compositions of mixed clays,
- Studying the thermal stabilities of inorganic compounds,
- Critically examining in a specific reaction whether a new compound is actually formed or the product is nothing but an unreacted original substance

- DTA offers a wide spectrum of useful investigations related to reaction kinetics, polymerization, solvent retention, phase-transformations, solid-phase reactions and curing or drying properties of a product.

3.3.3 (f) Advantages and disadvantages of Thermogravimetric analysis.

Advantages:

- Thermogravimetric analysis (TGA) **can simulate roasting conditions and produce a small sample for chemical analysis or materials characterization**.
- A simultaneous thermogravimetric and differential scanning calorimetry can identify endothermic and exothermic reaction temperatures **[53].**

Disadvantages :

The primary limitation of TGA methods, namely that **mass loss of volatiles is not equivalent to formation of degradants**, significantly impedes its ability to provide consistent universal indicators of actual extent of degradation **[54].**

3.3.3 (g) Advantages and disadvantages of Differential thermal analysis.

Advantages:

- Differential thermal analysis can also be used to measure two inert samples when their responses to the heat cycle are not identical.
- In these specific cases, DTA can also be used to identify any phase changes that are not based around a change in enthalpy.

Disadvantages:

- Due to heat variation between sample and reference makes it less sensitive.
- Change in temperature is not so accurate

3.3.4 RAMAN SPECTROSCOPY

- Raman spectroscopy is a molecular spectroscopic technique that utilizes the interaction of light with matter to gain insight into a material's make up or characteristics, like FTIR.

- The information provided by Raman spectroscopy results from a light scattering process, whereas IR spectroscopy relies on absorption of light.
- Raman spectroscopy yields information about intra- and inter-molecular vibrations and can provide additional understanding about a reaction.

3.3.4 (a) Principle

When light interacts with molecules in a gas, liquid, or solid, the vast majority of the photons are dispersed or scattered at the same energy as the incident photons. This is described as elastic scattering, or Rayleigh scattering.

A small number of these photons, approximately 1 photon in 10 million will scatter at a different frequency than the incident photon. This process is called inelastic scattering, or the Raman effect **[55].**

3.3.4 (b) Instrumentation of Raman spectroscopy.

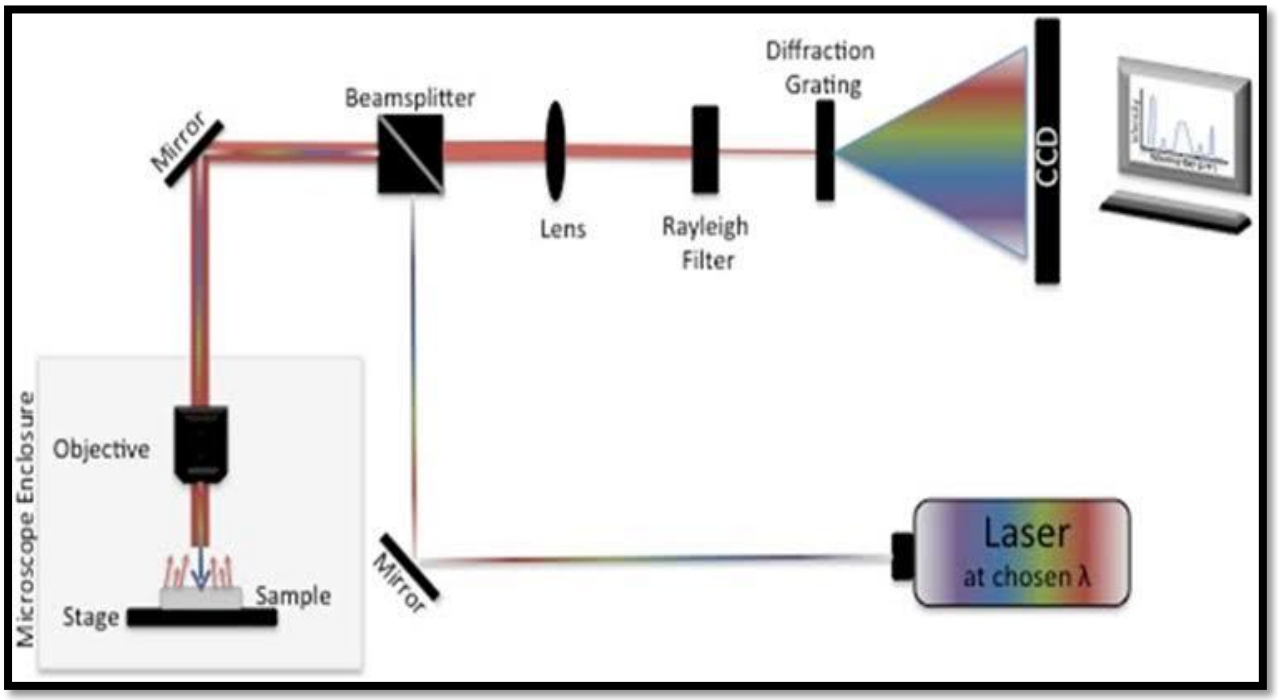

Figure:3.8 Raman Spectroscopy

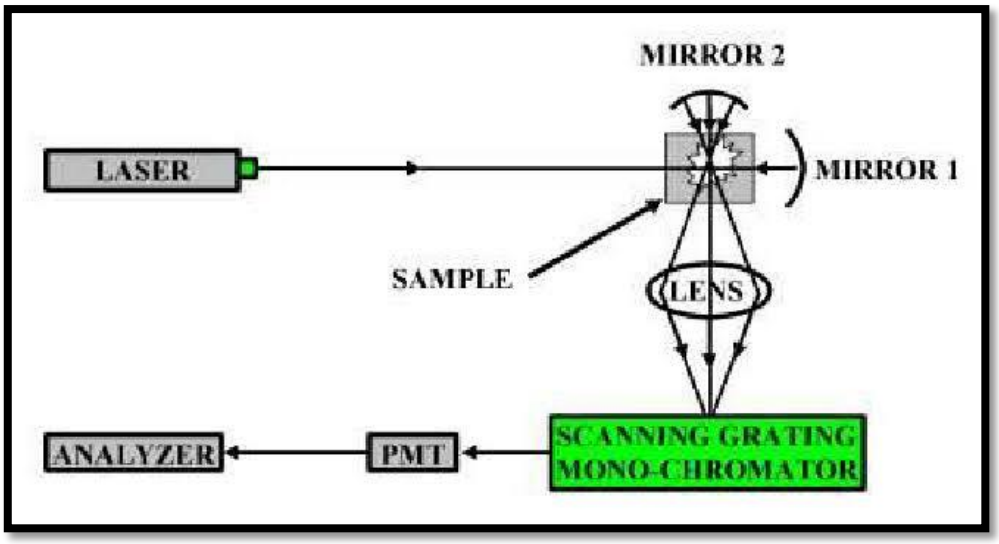

Figure 3.9 Instrumentation of Raman Spectroscopy

- A Raman spectrometer includes three main components such as the laser, the sampling interface, and the spectrometer itself.
- A typical Raman laser will consist of different characteristics, such as a small form factor, low power consumption, narrow line width, a stable power output, and a stable wavelength output.
- The second component includes the sampling interface. In many Raman spectrometers, fiber-optic probe is typically used which offers an extremely flexible sampling interface.
- These fiber-optic probes can be easily adapted to a range of optical microscopes, gas flow cells, liquid flow cells, and other sampling chambers. One critical aspect of a fiber-optic probe is a high-optical-density Raman cutoff.
- This means, when users are looking at the Raman spectrum, they need to ensure that the laser wavelength is blocked as much as possible so that the Raman shift can be observed.
- It is extremely important that the Raman shift is observed very close to the laser line since many materials have vital spectral features very near to the line.
- The third component is the spectrometer. Here, important performance factors are small form factor, high resolution, low power consumption, and low noise. An appropriate detector is very important and must be utilized depending on which excitation laser is being used.

3.3.4 (c) Applications of Raman Spectroscopy

- Raman is used in variety of applications. It can be used to identify explosives such as RDX, PETN, TNT, etc. and also the binding agents inside explosive materials.
- The technique is also effective for identifying toxic solvents in biowarfare agents and for studying other potentially harmful agents. Unlike FTIR spectroscopy, Raman is immune to aqueous absorption bands.

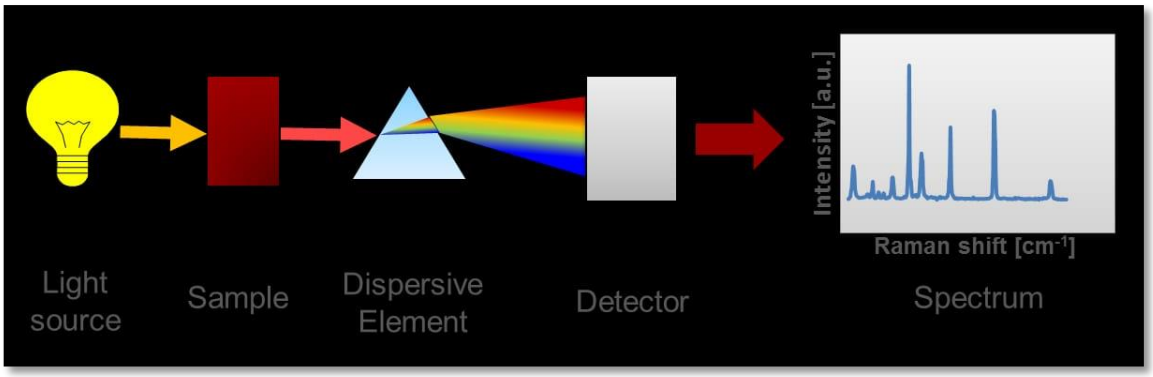

Figure 3.10 Raman Spectroscopy application

- In the pharmaceutical industry, one major application for Raman is the detection and substantiation of incoming raw materials.
- The technique is employed for the analysis of liquids, tablets, and gel caps.
- Raman is also an essential tool in counterfeit-drug analysis **[56].**

3.3.4 (d) Advantages of Raman spectroscopy.

- Many organic and inorganic materials are suitable for Raman analysis. These can be solids, liquids, polymers or vapors.
- No sample preparation needed.
- Not interfered by water.
- Non-destructive.
- Highly specific like a chemical fingerprint of a material.
- Raman spectra are acquired quickly within seconds.
- Samples can be analyzed through glass or a polymer packaging.

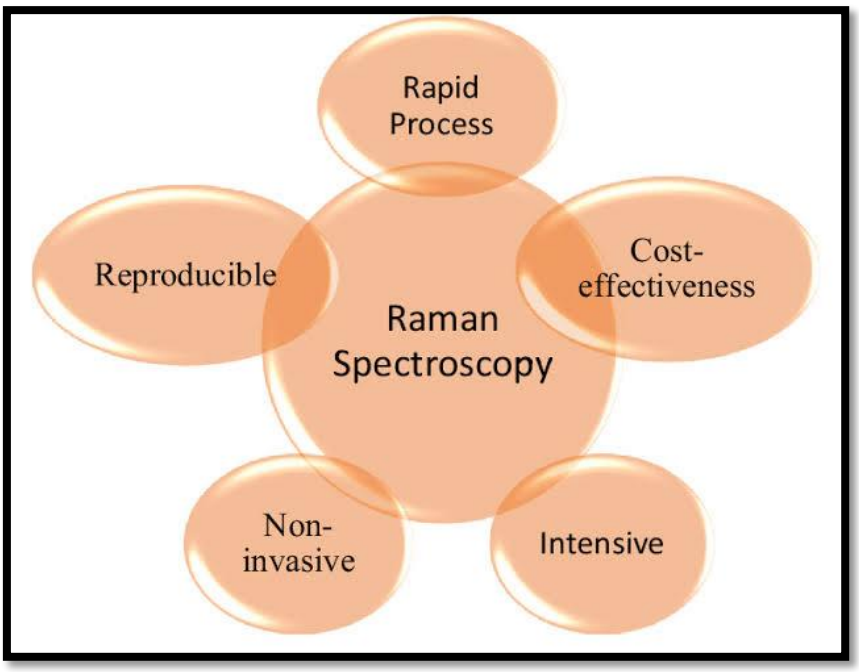

Figure 3.11 Advantages of Raman Spectroscopy

3.3.4 (e) Disadvantages of Raman spectroscopy.

- Cannot be used for metals or alloys.
- The Raman effect is very weak. The detection needs a sensitive and highly optimized instrumentation.
- Fluorescence of impurities or of the sample itself can hide the Raman spectrum.
- Some compounds fluoresce when irradiated by the laser beam.
- Sample heating through the intense laser radiation can destroy the sample or cover the Raman spectrum **[57].**

3.3.5 CYCLIC VOLTAMMETRY (CV)

- **Cyclic voltammetry** is an electrochemical technique for measuring the current response of a redox active solution to a linearly cycled potential sweep between two or more set values.
- It is a useful method for quickly determining information about the thermodynamics of redox processes, the energy levels of the analyte and the kinetics of electronic-transfer reactions **[58].**

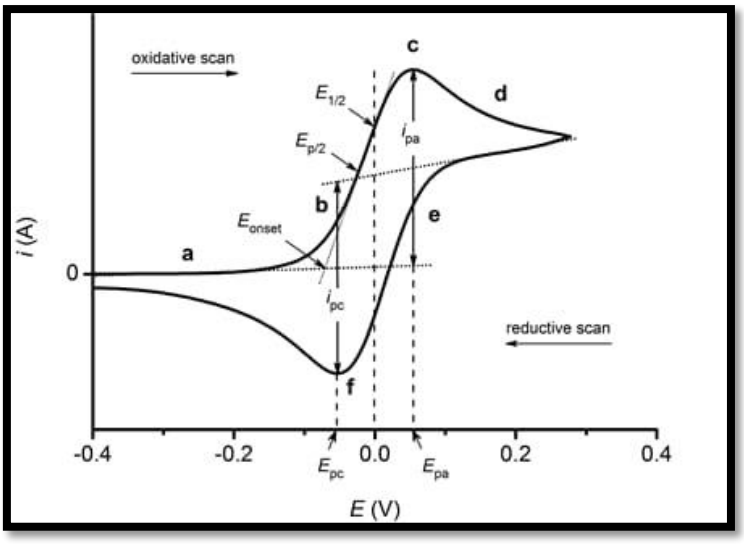

Figure: 3.12 Duck-shaped cyclic voltammogram

3.3.5 (a) Principle of CV

Cyclic voltammetry is a sophisticated potentiometric and voltammetric method. During a scan, the chemical either loses an electron (oxidation) or gains an electron (reduction) depending on the direction of the ramping potential.

3.3.5 (b) Instrumentation and working of CV

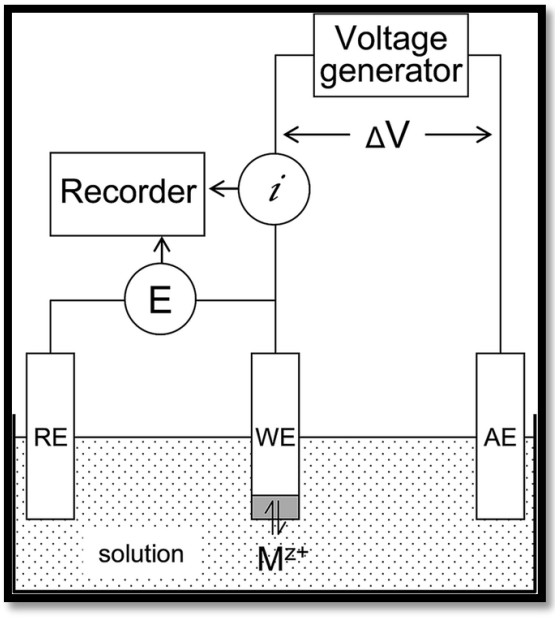

Figure: 3.13 Schematic representation of cyclic voltammetry

- A CV system consists of an electrolysis cell, a potentiostat, a current-to-voltage converter, and a data acquisition system. The electrolysis cell consists of a working electrode, counter electrode, reference electrode, and electrolytic solution.
- The working electrode's potential is varied linearly with time, while the reference electrode maintains a constant potential. The counter electrode conducts electricity from the signal source to the working electrode.
- The purpose of the electrolytic solution is to provide ions to the electrodes during oxidation and reduction. A potentiostat is an electronic device which uses a dc power source to produce a potential which can be maintained and accurately determined, while allowing small currents to be drawn into the system without changing the voltage.
- The current-to-voltage converter measures the resulting current, and the data acquisition system produces the resulting voltammogram.

3.3.5 (c) Applications of CV

- Cyclic Voltammetry can be used to study qualitative information about electrochemical processes under various conditions, such as the presence of intermediates in oxidation-reduction reactions, the reversibility of a reaction.
- CV can also be used to determine the electron stoichiometry of a system, the diffusion coefficient of an analyte, and the formal reduction potential, which can be used as an identification tool.
- In addition, because concentration is proportional to current in a reversible, Nernstian system, concentration of an unknown solution can be determined by generating a calibration curve of current vs. concentration **[59].**

3.3.5 (d) Advantage of CV

The advantage of using a smaller electrode is that **flatter more stable peak currents are obtained at faster scan rates [60].**

3.3.5 (e) Disadvantage of CV

Fast scan cyclic voltammetry seems to be the best available tool for sensing neurochemicals while providing excellent sensitivity and specificity, then why do scientists bother developing new surface electrode with different materials while using other voltammetries **[61]**

CHAPTER 4
RESULTS AND DISCUSSION

4.1 INTRODUCTION

This chapter deals with the characterization of the prepared sodium iron phosphate ($NaFePO_4$), and Zirconium doped $NaFePO_4$, ($NaFe_{0.98}Zr_{0.02}PO_4$) sample. The thermal, structural, vibrational, morphological and electrochemical behaviour of the prepared samples is discussed in this chapter.

4.2 Structural characterization

4.2.1 Thermogravimetric-Differential thermal analysis (TG-DTA)

The weight loss of precursor takes place in multistage process, and the thermal analysis of the sample is carried out using the instrument TG/DTA-EXSTAR/6300 (Thermo Gravimetric Analyser). The total weight loss of the precursor material is 63.56% as shown in the Figure 4.1.

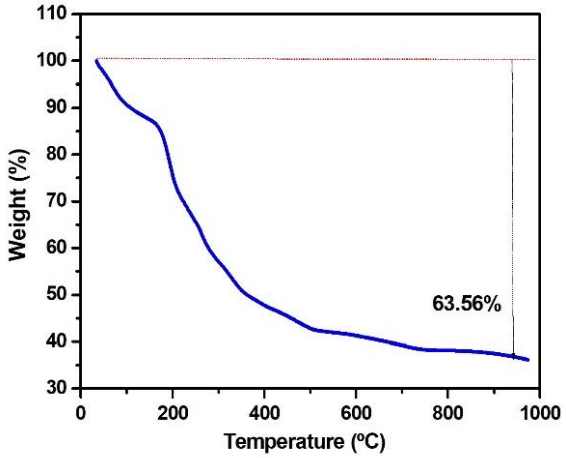

Figure 4.1: TG curve of precursor ($NaFePO_4$)

Figure 4.1 and 4.2 shows the thermogravimetric profiles of the precursor sample and this temperature dependent analysis is used to evaluate the possible reactions occurring at the time of synthesis of $NaFePO_4$ and is used to fix the calcination temperature for the preparation of expected product.

The TGA curves can be divided into five parts such as (RT) - 100ºC, 100ºC - 173ºC, 173ºC - 265ºC, 265ºC - 339ºC, 339ºC - 483ºC, 483ºC - 746ºC and 746ºC - 1000ºC regions. The

first stage of TG-DTA curve at (RT)- 100ºC, the weight loss observed in the sample is 9.5% which is related to the process of losing absorbed water (i.e., evaporation of moisture).

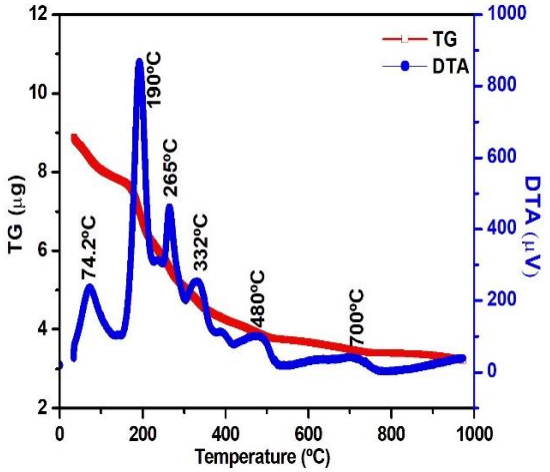

Figure 4.2: TG-DTA curve of precursor ($NaFePO_4$)

The stage of weight loss ranging from 339 ºC -483ºC correspond to the decomposition of citric acid complexes. The next weight loss region from 100 ºC to 339 ºC [62] attribute to the dehydration and decomposition ferrous oxalate dihydrate.

From the DTA curve the peaks observed at 190 ºC and 265 ºC corresponds to the ferrous oxalate decomposition, and the peak observed at 332 ºC may be due to the decomposition of Ammonium dihydrogen phosphate. In another report at 370 ºC and 495 ºC prominent weight gain is observed, corresponds to the oxidation of iron from Fe^{2+} to Fe^{3+} which is not observed in our case [63].

The region 480 ºC- 700 ºC shows a stable region of 8.14% residue after which the sample decomposes completely. From the DTA curve, an obvious endothermic peak at 700 ºC is obtained, is caused by the $NaFePO_4$ formation. The weight remains stable after 700 ºC, so in order avoid the overgrowth of $NaFePO_4$ particles, the optimized calcination temperature at 700 ºC is chosen and the same temperature of calcination is set for Zr doped $NaFePO_4$.

4.2.2 X-Ray Diffraction (XRD) analysis

X-Ray diffraction measurements are performed to investigate the crystallographic structure of the prepared samples $NaFePO_4$ and $NaFe_{0.98}Zr_{0.02}PO_4$. The X-ray diffraction pattern are obtained using the instrument PANanlytical XPert Pro. The XRD pattern of the

prepared samples $NaFePO_4$ and $NaFe_{0.98}Zr_{0.02}PO_4$ by sol gel method is shown in the Figure 4.3 and Figure 4.4.

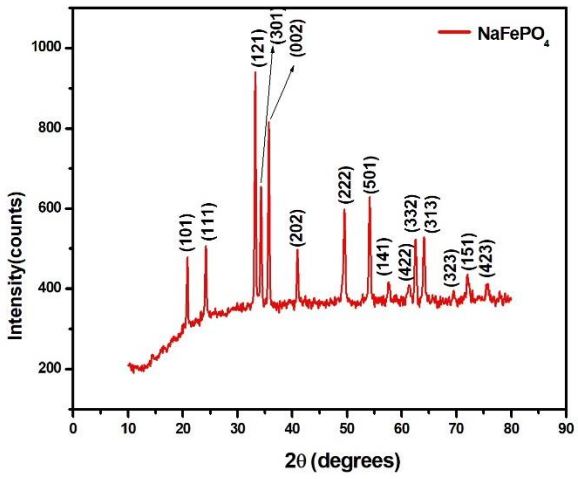

Figure 4.3: X-ray diffraction pattern of $NaFePO_4$

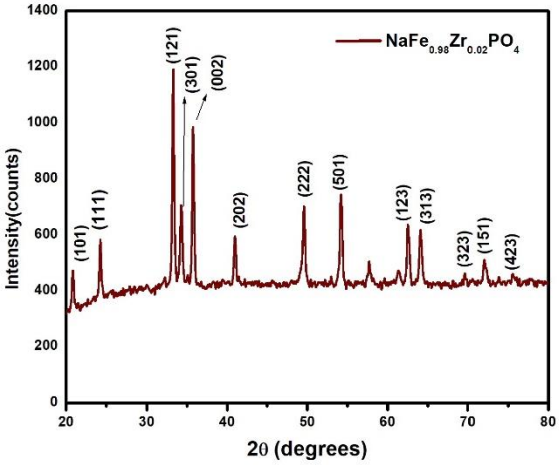

Figure 4.4: X-ray diffraction pattern of $NaFe_{0.98}Zr_{0.02}PO_4$

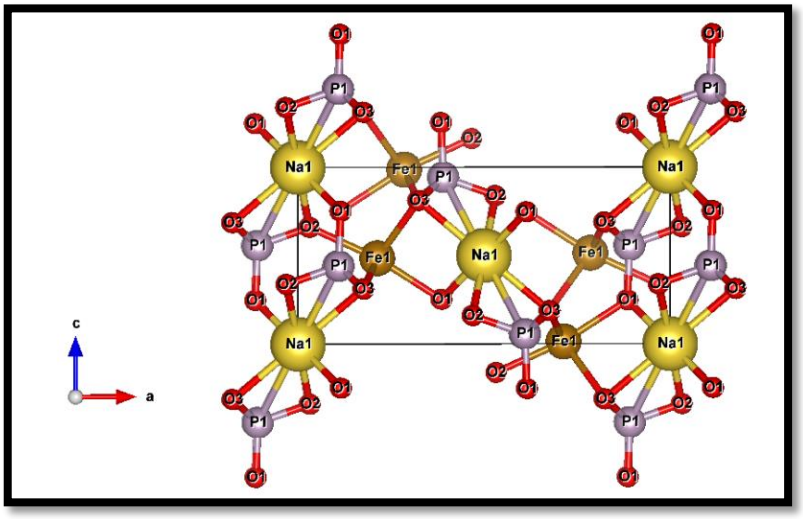

Figure 4.5: Structure of $NaFePO_4$ drawn using VESTA software

From the Figure 4.3, the diffraction peaks at 2θ values 20.8°, 24.1°, 33.2°, 34.3°, 35.7°, 41°, 49.6°, 54.1°, 57.6°, 61.4°, 62.5°, 64.1°, 69.5°, 72.1°, 75.6° are related to (101), (111), (121), (301), (002), (202), (222), (501), (141), (442), (123), (313), (323), (151), (423) hkl planes, and from the Figure 4.4 ($NaFe_{0.98}Zr_{0.02}PO_4$) the diffraction peaks at 2θ values 20.8°, 24.2°, 32.4°, 33.2°, 34.4°, 35.7°, 40.9°, 49.5°,54.2°, 57.7°, 61.4°, 62.5°, 64.1°, 69.6°, 72.1°,

75.6° were related to (101), (111), (220), (121), (301), (002), (202), (222), (501), (141), (442), (123), (313), (323),(151), (423) hkl planes respectively.

Figure 4.3 ($NaFePO_4$) exposed the sharp intense peak at 2θ = 33.2°, 35.7° which corresponds to the miller indices (121), (002) and the same results are obtained for the doped sample [64]. The results confirm that orthorhombic structure with pnma space group and it is matched well with the standard value of JCPDS Card No. 89-0816.

The ionic radii of the dopant Zr^{4+} is 0.8 Å. Replacement of Zr^{4+} in the place of Iron (Fe) is aimed during synthesis, and the ionic radii compatibility is ensured. The lattice parameters of the pure $NaFePO_4$ sample are a=8.017 Å, b=6.590 Å, c=4.9919 Å. The unit cell volume calculated for the pure sample is 273.45 $Å^3$ whereas the lattice parameters of $NaFe_{0.98}Zr_{0.02}PO_4$ are a=7.8714 Å, b=6.590 Å and c=4.9919 Å, and the volume of the Zr doped sample is 259.25 $Å^3$. The lattice parameters and the unit cell volume are decreased in the case of doping. Upon doping of Zr into the host matrix, there are remarkable changes observed in the lattice parameters and also the volume of the cell. This gives a clear indication that the Zr doped occupies interstitial position in the host matrix.

The crystallite size D, can be estimated from the peak width using Scherrer's formula. The Debye Scherrer formula is,

$$\mathbf{L}=\frac{k\lambda}{\beta cos\theta}\ \text{nm}$$

Where,

λ = X-ray wavelength (0.154 nm)

β = Full width half maximum (FWHM) of a diffraction peak (radians)

θ = diffraction angle,

k = Scherrer's constant of the order of unity (0.9).

The calculated values of FWHM, d-spacing, crystallite size and strain values are given in Table 4.1.

The crystallite size of doped sample remains higher than the pure $NaFePO_4$. In spite of the increase in the crystallite size on addition of dopant, the strain gets decreased.

Strain parameter is always inversely proposed to the crystallite size.

Table 4.1: Calculated parameters from XRD of $NaFePO_4$ and $NaFe_{0.98}Zr_{0.02}PO_4$

Samples	**$2\theta_{(121)}$ (deg)**	**β (FWHM) (deg)**	**$D_{(121)}$ (Å)**	**Crystallite size $D_{(121)} = \frac{K\lambda}{\beta cos\theta}$ nm**	**Strain Ɛ**	**Volume ($Å^3$)**
$NaFePO_4$	33.24	0.2007	2.690	41.3	0.1732	273.45
$NaFe_{0.98}Zr_{0.02}PO_4$	33.24	0.1673	2.596	49.56	0.1444	259.25

Table 4.2: Indexing planes of $NaFePO_4$

No. of. Peaks	**2θ (deg)**	**H**	**k**	**l**	**$1/d^2$**
1.	33.24	1	2	1	0.0985
2.	35.75	0	0	2	0.0793
3.	34.31	3	0	1	0.0863
4.	54.16	5	0	1	0.1174
5.	49.50	2	2	2	0.1537
6.	24.20	1	1	1	0.0768
7.	20.85	1	0	1	0.0552
8.	64.12	3	1	3	0.1873
9.	62.62	1	2	3	0.1778
10.	41.00	2	0	2	0.1104
11.	72.15	1	5	1	0.1636
12.	57.68	1	4	1	0.1419
13.	75.66	4	2	3	0.2245

Table 4.3: Indexing planes for $NaFe_{0.98}Zr_{0.02}PO_4$

No. of. Peaks	2θ (deg)	H	k	l	$1/d^2$
1.	33.2474	1	2	1	0.10231
2.	35.7521	0	0	2	0.08025
3.	54.1368	5	0	1	0.12082
4.	34.2610	3	0	1	0.08854
5.	49.5834	2	2	2	0.15858
6.	62.5084	1	2	3	0.18257
7.	24.2585	1	1	1	0.07929
8.	64.0642	3	1	3	0.19182
9.	40.9651	2	0	2	0.11253
10.	20.8069	1	0	1	0.05626

4.3 Raman analysis

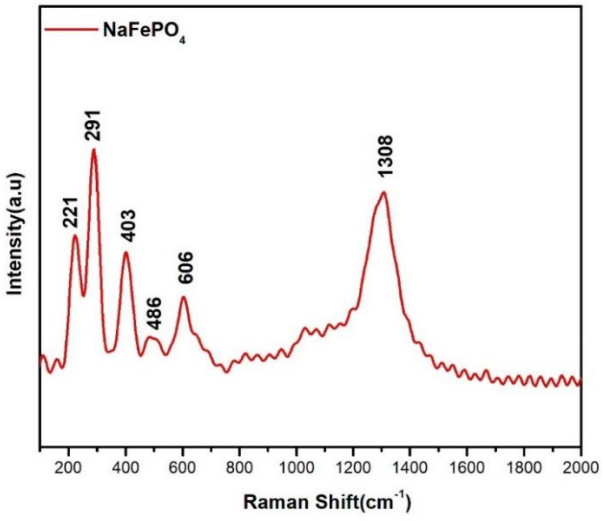

Figure 4.6: Raman spectra of $NaFePO_4$

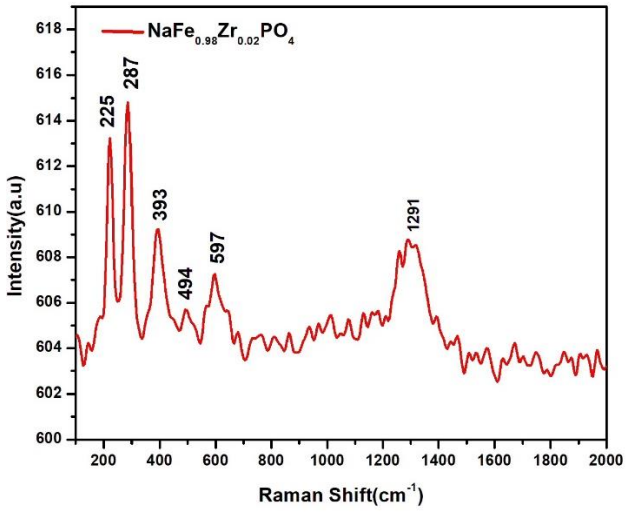

Figure 4.7: Raman spectra of $NaFe_{0.98}Zr_{0.02}PO_4$

From the Raman spectra of $NaFePO_4$ (Figure 4.6), peaks at 221, 291, 403, 606 and 1308 cm^{-1} and $NaFe_{0.98}Zr_{0.02}PO_4$ (Figure 4.7) peaks at 225, 287, 393, 597, 1291 are assigned to various vibrational modes as follows. The similarity of the positions and patterns of characteristic Raman peaks are seen and the peak located at 403 cm^{-1} Figure 4.6 of $NaFePO_4$ showed peaks at 393 cm^{-1} (Figure 4.7) of $NaFe_{0.98}Zr_{0.02}PO_4$ and are attributed to the deformation of PO_4^{3-} structural units [66]. Obvious evolution of the characteristic peaks in the region 200 ~ 400 cm^{-1} is seen, the other two peaks at 221and 291 cm^{-1} (Figure 4.6) of $NaFePO_4$ and 225, 287 cm^{-1} (Figure 4.7) of $NaFe_{0.98}Zr_{0.02}PO_4$ corresponds to the FeO vibrations [65]. The Raman shift appeared in the range of 489 cm^{-1} (Figure 4.6) of $NaFePO_4$ and 494 cm^{-1} (Figure 4.7) of $NaFe_{0.98}Zr_{0.02}PO_4$ also belongs to Fe-O vibrations. The peak at 606 cm^{-1} in (Figure 4.6) $NaFePO_4$ and , 597 cm^{-1} in (Figure 4.7) $NaFe_{0.98}Zr_{0.02}PO_4$ corresponds to the intramolecular stretching mode of PO_4^{3-} [67]. This preservation of local coordination surroundings in P should arise from the stable and strong P-O covalent bonds. The peak at 1308 cm^{-1} corresponds to P=O stretching vibration and this peak position has been shifted to lower wavenumber 1291 cm^{-1} in case of doped sample. These characterization bands further confirm the formation of phosphate radicals [68].

4.4 Morphological analysis

4.4.1 Field Emission Scanning Electron Microscopy (FESEM)

The morphological facts of the prepared samples $NaFePO_4$, $NaFe_{0.98}Zr_{0.02}PO_4$ are examined using Field Emission Scanning Electron Microscopy (FESEM) and horizontal plates like morphology was observed `in the pure $NaFePO_4$ sample. Upon doping, the particles seems to be agglomerated in the case of Zr-doped sample.

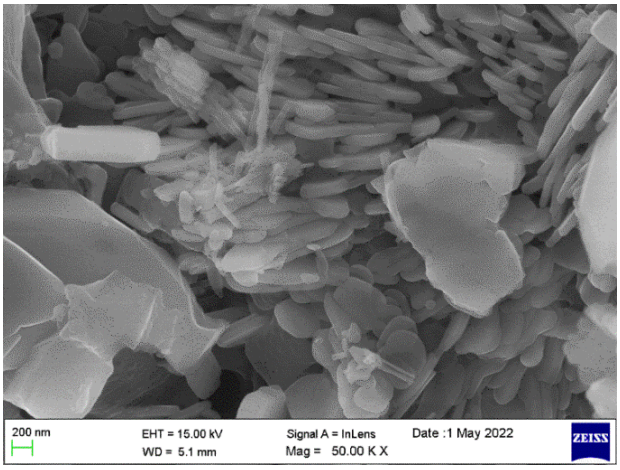

Figure 4.8: FESEM image of $NaFePO_4$

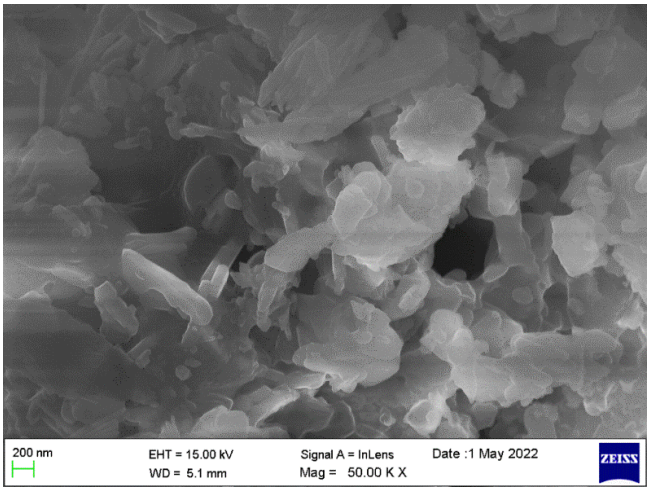

Figure 4.9: FESEM image of $NaFe_{0.98}Zr_{0.02}PO_4$

4.5 Cyclic Voltammetry (CV) analysis

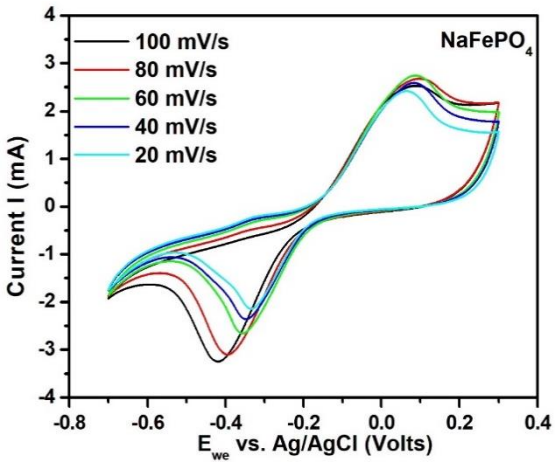

Figure 4.10: CV curve of $NaFePO_4$

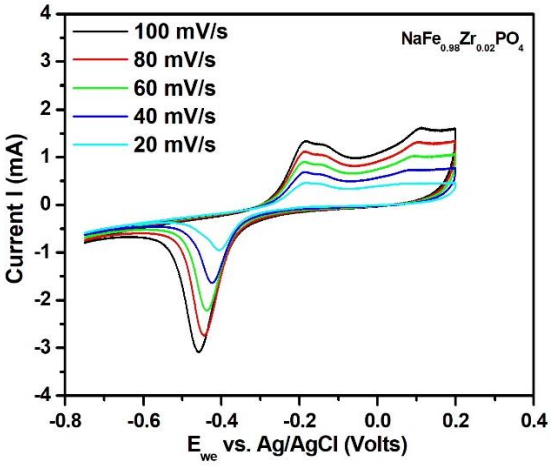

Figure 4.11: CV curve of Zr-doped $NaFePO_4$

The specific capacitance is calculated using the formula,

$$C_{sp} = \int_{E1}^{E2} i(E)dE/(E_2 - E_1)mv$$

Where, $\int_{E1}^{E2} i(E)dE$ is the integrated area of the instantaneous current over the range of cut off potentials E_1 and E_2 and (E_2-E_1) is the working potential window of the electrochemical system, m is the mass of the working electrode in g and v is scan rate in V/sec.

The specific capacitance value of pure $NaFePO_4$ is 14.3 mAh/g and the Zr-doped sample exhibits a value of 9.2 mAh/g.

Hence, Zr-doped sample shows lower value of specific capacitance than the pure sample.

This is due to the decrease in the integral area of the CV curve of the Zr-doped sample since the specific capacitance is directly proportional to the integral area of the CV curve.

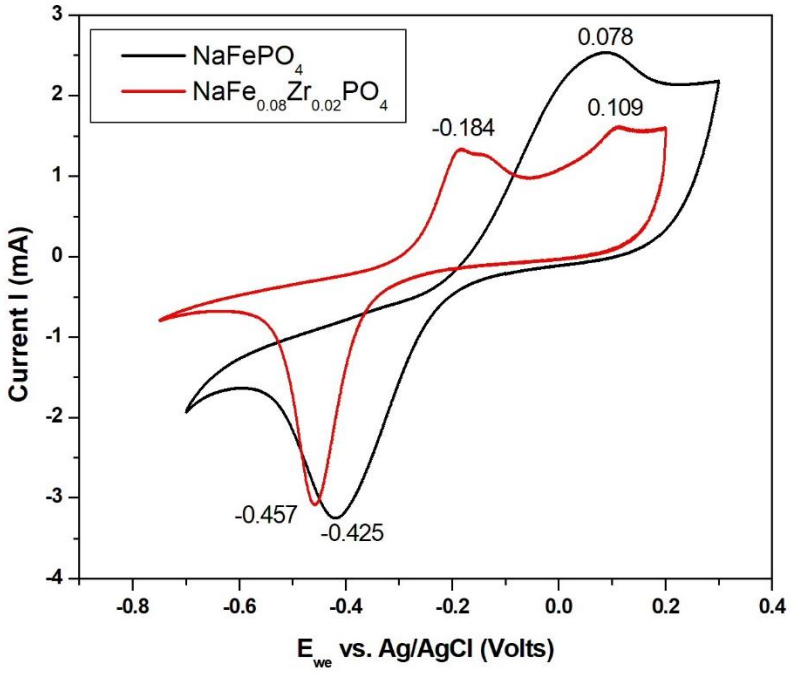

Figure 4.12: Comparison of CV curve of pure and Zr doped samples

From the Figure 4.12 the potential window of the prepared $NaFePO_4$ lies between -0.7 to +0.3 V, whereas in the case of doped sample it is extended from -0.75 to +0.2 V.

The oxidation and reduction peaks of pure sample is 0.078 and -0.425 V and for the doped sample there exists two oxidation peaks at -0.184 V and 0.109 V and reduction potential at -0.457 respectively.

The reduction potential of -0.420V of the pure sample shows the iron reduction process. The potential observed at -0.184V for the doped sample may be due to the reduction of iron.

$$Fe\ OH^{+}+H^{+}+2e^{-} \rightarrow Fe(S) + H_20\ (Evolved\ hydrogen)$$

Second oxidation peak 0.1098V may be due to the presence of phosphorous.

Since, the copper leaching occurs in the Zr^{+} doped sample, to reap the advantage of operative window in this case, it is recommended to use substrate other than copper.

The parameters calculated from the CV graph is shown in Table 4.4 and 4.5.

Table 4.4: CV analysis parameters of $NaFePO_4$ in 1M-NaOH electrolyte

Scan rate (mV/s)	**Potential (V)**			**Current (mA)**		
	Epa	**Epc**	**|Epa-Epc|**	**Ipa**	**Ipc**	**|Ipc/Ipa|**
100	0.079	-0.419	0.498	1.893	-2.094	1.8114
80	0.087	-0.391	0.478	1.94	-2.004	1.8152
60	0.082	-0.358	0.44	1.916	-1.674	1.7510
40	0.075	-0.348	0.423	1.739	-1.415	1.5757
20	0.059	-0.335	0.394	1.563	-1.325	1.6965

Table 4.5: CV analysis parameters of $NaFe_{0.98}Zr_{0.02}PO_4$ in 1M-NaOH electrolyte

Scan rate (mV/s)	**Potential (V)**			**Current (mA)**		**|Ipc/Ipa|**
	Epa	**Epc**	**|Epa-Epc|**	**Ipa**	**Ipc**	
100	-0.188	-0.459	0.271	1.323	-3.075	2.324
80	-0.186	-0.445	0.259	1.098	-2.731	2.487
60	-0.1887	-0.438	0.249	0.892	-2.201	2.467
40	-0.1887	-0.424	0.235	0.681	-1.631	2.395
20	-0.1816	-0.405	0.223	0.461	-0.948	2.056

Table 4.6: Review table on $NaFePO_4$ and its electrochemical performance

Author [Year Of Publication]	Material Used	Method of Preparation	Electrochemical Performance
Roman R. Kapaev et al., (2017) [26]	• Maricite-type $NaFePO_4$ as a cathode material	Solid state method	• $NaFePO_4$ exhibits capacity up to 150 mAh g^{-1}
Fangyu Xiong et al., (2018) [23]	• Sodium metal anode • $NaFePO_4$ as highly active cathode material	Electro-spinning technique	• Reversible capacity of 142 mAh g^{-1} at 0.05 C at the first cycle and an outstanding cyclability with a 95% retention after 200 cycles
F Rahmawati et al., (2020) [16]	• Graphite/Cu foil layer as anode • $NaFePO_4$ as cathode	Electrochemical sodiation to $FePO_4$ layer on aluminium substrate	• $NaFePO_4$ cathode delivered a good specific capacity near 154 mAh/g
Duan Wang et al., (2020) [18]	• $NaFePO_4$ nanoparticles encapsulated within ultrathin carbon coating (NFP@NPCM) used as cathode material	Sol-gel method	• The discharge **specific capacity** after five cycles is as high as 140 mA h g^{-1} , which is 91% of the theoretical capacity (155 mA h g^{-1}) of $NaFePO_4$
Bingqiu Liu et al., (2021) [12]	Maricite $NaFePO_4$ (NFP) as cathode	Facile method	• Exhibit high capacity of 149.2 mA h g^{-1} at 0.2C and Outstanding cycling performance (91.3 mA h g^{-1} at 10C after 5000 cycles with 95.0% retention).

A.J. Fernandez-Ropero et al., (2019) [20]	Nasicon type $Na_2FeP_2O_7$ as cathode	Electrochemical delithiation-sodiation method	• Capacity achieved about 110 mAh g^{-1} at C/10 and 74 mAh g^{-1} at 2 C.
C. Heubner et al., (2017) [30]	$NaFePO_4$ as cathode	Electrochemical alkali metal cation displacement technique	• Submicron sized $NaFePO_4$ having 80 % of the theoretical capacity of (154 mAh g^{-1}).
Pier Paolo Prosini et al., (2014) [37]	$NaFePO_4$ as cathode	Hydrothermal method and solid-state synthesis	• Specific capacity of 125 mAh g^{-1} over 50 charge–discharge at room temperature and under a very low charge–discharge rate (C/20).
This work	Pure $NaFePO_4$ $NaFe_{0.98}Zr_{0.02}PO_4$	Sol-gel method	• Specific capacitance value of 14.3 $mAhg^{-1}$ for pure sample and 9.2 $mAhg^{-1}$ for Zr-doped sample.

The lower value of specific capacitance may be due to the effect of substrate and could be improved by the use of substrate other than copper. And a direct comparison cannot be made with other reports, because an aqueous electrolyte medium is used in our case whereas in other reports organic electrolytes are used.

The preliminary testing of the pure and doped sample are studied in the present work. By improvisation of structural properties of the doped sample and by the effective use of suitable substrate, the electrochemical performance could be improved and used as cathode for sodium ion batteries.

CHAPTER V

SUMMARY AND CONCLUSION

The effect of zirconium as dopant in Sodium iron phosphate ($NaFePO_4$) is evaluated in the present study. Herein, $NaFePO_4$ and Zr-doped $NaFePO_4$ are synthesized by sol-gel method and its thermal, structural, morphological and electrochemical properties are studied. From the thermogravimetric analysis, the weight loss of the precursor ($NaFePO_4$) takes place in a multistage process. The total weight loss of the precursor of $NaFePO_4$ material is 63.56% and from the DTA curve, the calcination temperature of 700 °C is chosen for the preparation of both pure and the doped samples. The crystal structure of the prepared samples are analysed by powder X-ray diffraction technique. All the X-ray diffraction pattern of the prepared samples are indexed to ordered orthorhombic structure with pnma space group. Upon doping Zr^{4+} in the Fe site of $NaFePO_4$, the crystallite size has been increased and strain is decreased. Thus, the Zr doped $NaFePO_4$ is supposed to occupy the interstitial position in the host matrix. The local structure of $NaFePO_4$ and Zr doped $NaFePO_4$ are analysed by laser Raman spectroscopy and the characterization bands further confirm the formation of phosphate radicals of $NaFePO_4$. The morphological facts of the prepared samples are identified by Field emission scanning electron microscopy. In the case of pure sample ($NaFePO_4$) horizontal plates like morphology was observed and agglomerated in the case of Zr doped sample. The specific capacity of the pure $NaFePO_4$ is 14.3 mAh/g and the Zr doped $NaFePO_4$ exhibits 9.2 mAh/g. By further investigation of the structure and its other electrochemical properties, the prepared doped material could be effectively used as cathode material for sodium-ion batteries.In the present ratio of doping, the occupation of Zr could be on A site. If it is made to occupy in the B site, a broader caging is possible for Na mobility. Futuristic scope is to allow Zr at higher concentration and at different occupancies and search the spectrum of dopant for better performance.

LIST OF REFERENCES

[1] Dr. Dipan Kundu,Elahe Talaie,Dr. Victor Duffort,Prof. Linda F. Nazar, The Emerging Chemistry of Sodium Ion Batteries for Electrochemical Energy Storage**,** vol-54, Issue-11, 3431-3448, March 9, 2015. DOI: 10.1002/anie.201410376

[2] Sodium-Ion Battery,European Association for storage of energy,2020. 10.3030/963542

[3] Winter, Martin; Brodd, Ralph J. (2004). What Are Batteries, Fuel Cells, and Supercapacitors? , 104(10), 4245–4270. https://doi.org/10.1021/cr020730k

[4] Jose Alarco And Peter Talbot**,** The history and development of batteries Jose Alarco And Peter Talbot**,** April 30 2015.

[5] Emmanuel odunlade, Different Types of Batteries and their Applications, July 24, 2018

[6] https://www.vedantu.com/chemistry/battery-types

[7]https://www.saftbatteries.com/media-resources/our-stories/three-battery-technologies-could-power-future

[8] Jang-Yeon Hwang, Seung-Taek Myung and Yang-Kook Sun Sodium-ion batteries: present and future, Chem. Soc. Rev.**,** 2017,46**,** 3529-3614 DOI:10.1039/C6CSOO776G

[9] B.T.S. Ramanujam, Ashok Kumar Nanjundan, Pratheep K. Annamalai, Nanocellulose-based carbon as electrode materials for sodium-ion batteries, Micro and Nano Technologies, 295-312,2021 https://doi.org/10.1016/B978-0-12-822350-5.00012-6.

[10] Duygu karabelli, soumya singh, Stephen keimel, Sodium-Based Batteries: In Search of the Best Compromise Between Sustainability and Maximization of Electric Performance, Front. Energy Res., 21 December 2020 https://doi.org/10.3389/fenrg.2020.605129

[11] https://www.grepow.com/blog/sodium-ion-vs-lithium-ion-battery-are-sodium-batteries-better/

[12]. **Bingqiu Liu , Qi Zhang , Lu Lia , Lingyu Zhang , Zhanshuang Jin , Chungang Wanga , Zhongmin Su**, Achieving highly electrochemically active maricite $NaFePO_4$ with

ultrafine $NaFePO_4$@C subunits for high rate and low temperature sodium-ion batteries, Electrochemical Engineering Journal,vol-405, 1, 126689, February 2021. https://doi.org/10.1016/j.cej.2020.126689

[13]. **M. Karthik, S. Sathishkumar , R. BoopathiRaja , K. L. Meganathan , and T. Sumathi,** Design and fabrication of $NaFePO_4$/MWCNTs hybrid electrode material for sodium-ion battery, Journal of material science: Materials in electronics, 31, pages 21792–21801, 2020. https://doi.org/10.1007/s10854-020-04691-y

[14]. **Rachid Essehli , Hamdi Ben Yahia, Ruhul Amin , Fadwa El-Mellouhi, Ilias Belharouak,** Selective sodium-ion diffusion channels in $Na_{2-x}Fe_3(PO_4)_3$ positive electrode for Na-ion batteries, Vol-24, January 2020, Pages 343-350. https://doi.org/10.1016/j.ensm.2019.07.040

[15]. **Yongjie Cao, Yao Liu, Deqiang Zhao, Xiuping Xia, LaiChang Zhang, Junxi Zhang, Haishen Yang, and YongYao Xia**, A Highly Stable $Na_3Fe_2(PO_4)_3$@Hard Carbon Sodium-Ion Full Cell for Low Cost Energy Storage, ACS Sustainable Chem. Eng, 8, 3, 1380–1387, 2020. http://dx.doi.org/10.1021/acssuschemeng.9b05098

[16]. **F Rahmawati, Z Faiz, D A N Romadhona, T E Saraswati and W W Lestari,** The performance of sodium ion battery with NaFePO4 cathode prepared from local iron sand, IOP Conf. Ser.: Mater. Sci. Eng. 902 012008, 2020. Doi:10.1088/1757-899X/902/1/012008

[17]. **Yongjie Cao , Xiuping Xia , Yao Liu , Ning Wang a , Junxi Zhang , Deqiang Zhao, Yongyao Xia,** Scalable synthesizing nanospherical $Na_4Fe_3(PO_4)2(P_2O_7)$ growing on MCNTs as a high-performance cathode material for sodium-ion batteries, Journal of power sources, vol-461, 228130, Jun 2020. https://doi.org/10.1016/j.jpowsour.2020.228130.

[18]. **Duan Wanga , Yuanbo Wu , Jinmeng Lv , Rongrong Wang , Sailong Xu,** Carbon encapsulated maricite $NaFePO_4$ nanoparticles as cathode material for sodium-ion batteries. Colloids and Surfaces A, vol-583, 123957, 20 December 2019. https://doi.org/10.1016/j.colsurfa.2019.123957

[19]. **Ganesh S. Shinde, Ritambhara Gond, Maxim Avdeev, Chris D. Ling, Rayavarapu Prasada Rao, Stefan Adams, Prabeer Barpanda**, Revisiting the layered $Na_3Fe_3(PO_4)_4$

phosphate sodium insertion compound: Structure, magnetic and electrochemical study, Materials Research Express, vol-7, 2019. https://doi.org/10.1016/j.cej.2020.126689

[20]. **A.J. Fernandez-Ropero , D. Saurel , B. Acebedo , T. Rojo a, M. Casas-Cabana,** Electrochemical characterization of $NaFePO_4$ as positive electrode in aqueous sodium-ion batteries, Journal of power sources, vol-291, 40-45, 30 September 2015. https://doi.org/10.1016/j.jpowsour.2015.05.006

[21]. **Mingzhe Chen , Weibo Hua, Jin Xiao, David Cortie , Weihua Chen, Enhui Wanz, Zhe Hu , Qinfen Gu , Xiaolin Wang , Sylvio Indris, Shu-Lei Chou & Shi-Xue Dou,** NASICON-type air-stable and all-climate cathode for sodium-ion batteries with low cost and high-power density, vol-10,2019. https://doi.org/10.1038/s41467-019-09170-5

[22]. **Jiexin Zhang, Xi Zhou, Yunxiao Wang, Jiangfeng Qian, Faping Zhong, Xiangming Feng, Weihua Chen, Xinping Ai, Hanxi Yang, and Yuliang Cao**, Highly Electrochemically-Reversible Mesoporous Na_2FePO_4F/C as Cathode Material for High-Performance Sodium-Ion Batteries. Small 2019, 1903723. https://doi.org/10.1002/smll.201903723

[23**]. Fangyu Xiong, Qinyou An, Lixue Xia, Yan Zhao, Liqiang Mai, Haizheng Tao, Yuanzheng Yue**, Revealing the atomistic origin of the disorder enhanced Na-storage performance in $NaFePO_4$ battery cathode, Nano Energy, vol-57, 608-615, March 2019. https://doi.org/10.1016/j.nanoen.2018.12.087

[24]. **Nina V. Kosova , Daria O. Rezepova , Olga A. Podgornova , Arseny B. Slobodyuk , Sergey A. Petrov , Maxim Avdeev,** A comparative study of structure, air sensitivity and electrochemistry of sodium iron pyrophosphates $Na_{2-x}Fe_{1+x/2}P_2O_7$, Electrochimica Acta ,vol-235, Pages 42-55, May 2017. https://doi.org/10.1016/j.nanoen.2018.12.087

[25]. **Jiechen Lu, Shin-ichi Nishimura and Atsuo Yamada,** A Fe-rich sodium iron orthophosphate as cathode material for rechargeable batteries, Electrochemistry Communications, Vol-79, 51-54, Jun 2017. https://doi.org/10.1016/j.elecom.2017.04.012

[26]. **Roman R. Kapaev, Andrey A. Chekannikov, Svetlana A. Novikova, Tatiana L. Kulova, Alexander M. Skundinc and Andrey B. Yaroslavtsev**, Mendeleev Commun, 27, 263–264, ., 2017. https://doi.org/10.1016/j.mencom.2017.05.015

[27]. **Mingzhe Chen, Lingna Chen, Zhe Hu, Qiannan Liu, Binwei Zhang, Yuxiang Hu, Qinfen Gu, Jian-Li Wang, Lian-Zhou Wang, Xiaodong Guo, Shu-Lei Chou, and Shi-Xue Dou,** Carbon-Coated $Na_{3.32}Fe_{2.34}(P_2O_7)_2$ Cathode Material for High-Rate and Long-Life Sodium-Ion Batteries, Advanced materials, vol-29, Issue-21, 29 March 2017. https://doi.org/10.1002/adma.201605535

[28]. **Ranjusha Rajagopalan, Bo Chen, Zhicheng Zhang, Xing-Long Wu, Yonghua Du, Ying Huang, Bing Li, Yun Zong, Jie Wang, Gwang-Hyeon Nam, Melinda Sindoro, Shi Xue Dou, Hua Kun Liu, and Hua Zhang,** Improved Reversibility of Fe3+/Fe4+ Redox Couple in Sodium Super Ion Conductor Type $Na_3Fe_2(PO_4)_3$ for Sodium-Ion Batteries, vol-29, Issue-12, March 28 2017. https://doi.org/10.1002/adma.201605694

[29]. **V. Priyanka, R.Subadevi, M.Sivakumar,** Synthesis And Structural Analysis of $NaFePO_4$ Nanocomposite For Sodium Ion Batteries, International Research Journal of Engineering and Technology (IRJET), vol-4, Issue-9, Sep 2017. https://doi.org/10.1016/j.colsurfa.2019.123957

[30]. **C. Heubnera , S. Heiden , M. Schneider**, A. Michaelis, In-situ preparation and electrochemical characterization of submicron sized NaFePO4 cathode material for sodium-ion batteries, vol-233, 78-84, 10 April 2017. https://doi.org/10.1016/j.electacta.2017.02.107

[31]. **Yao Liu, Yirong Zhou , Junxi Zhang , Shiming Zhang, Ping Ren,** The relation between the structure and electrochemical performance of sodiated iron phosphate in sodium-ion batteries, vol-314, 15 May 2016, Pages 1-9. https://doi.org/10.1016/j.jpowsour.2016.03.003

[32]. **Satoshi Nakata, Takuya Togashi, Tsuyoshi Honma , Takayuki Komatsu**, Cathode properties of sodium iron phosphate glass for sodium ion batteries, Journal of Non-Crystalline Solids, 450,109-115, 2016. https://doi.org/10.1016/j.jnoncrysol.2016.08.005

[33]. **Yao Liu, Yirong Zhou, Junxi Zhang, Yongyao Xia, Tong Chen, and Shiming Zhang,** A Monoclinic Phase $Na_3Fe_2(PO_4)_3$: Synthesis, Structure and Electrochemical Performance as Cathode Material in Sodium-ion Batteries, CS Sustainable Chem. Eng, 5, 2, 1306–1314, 2017. https://doi.org/10.1021/acssuschemeng.6b01536

[34]. **Xudong Ma, Jiuyang Xia , Xuehang Wu , Zhiyi Pan , Pei Kang shen,** Remarkable enhancement in the electrochemical activity of maricite $NaFePO_4$ on high-surface-area carbon cloth for sodium-ion batteries, vol-146, 78-87, May 2019. https://doi.org/10.1016/j.carbon.2019.02.004

[35]. **Yongjin Fang, Qi Liu, Lifen Xiao, Xinping Ai, Hanxi Yang, and Yuliang Cao,** A High-performance Olivine $NaFePO_4$ Microsphere Cathode Synthesized by Aqueous Electrochemical Displacement Method for Na Ion Batteries, ACS Appl. Mater. Interfaces, 7, 32, 17977–17984,2015. https://doi.org/10.1021/acsami.5b04691

[36]. **Tsuyoshi Honma , Atsushi Sato, Noriko Ito, Takuya Togashi, Kenji Shinozaki, Takayuki Komatsu,** Crystallization behavior of sodium iron phosphate glass $Na_{2-x}Fe_{1+0.5x}P_2O_7$ for sodium ion batteries, Journal of Non-Crystalline Solids, 404, 26-31, 2014. https://doi.org/10.1016/j.jnoncrysol.2014.07.028

[37]. **Pier Paolo Prosini, Cinzia Cento , Amedeo Masci , Maria Carewska,** Sodium extraction from sodium iron phosphate with a Maricite structure, vol-263, 1-8,2014. https://doi.org/10.1016/j.ssi.2014.04.019

[38].**Thrinathreddy Ramireddy, Md Mokhlesur Rahman, Neeraj Sharma, Alexey M. Glushenkov, Ying Chen,** Carbon coated $Na_7Fe_7(PO_4)_6F_3$: A novel intercalation cathode for sodium-ion batteries- Journal of Power Sources, 271 (2014), 497-503. https://doi.org/10.1016/j.jpowsour.2014.08.039

[39]. **Prabeer Barpanda, Guandong Liu, Chris D. Ling, Mao Tamaru, Maxim Avdeeev, Sai- Cheong Chung, Yuki Yamada, and Atsuo Yamada,** $Na_2FeP_2O_7$: A Safe Cathode for Rechargeable Sodium ion Batteries,Chem. Mater. (2013), 25, 3480- 3487. https://doi.org/10.1021/cm401657c

[40]. **P. Moreau, D. Guyomard, J. Gaubicher, and F. Boucher,** Structure and Stability of Sodium Intercalated Phases in Olivine $FePO_4$, Chem. Mater, 22, 4126–4128, 2010. https://doi.org/10.1021/cm101377h

[41]. **Yongjie Cao, Yao Liu , Deqiang Zhao, Junxi Zhang, Xiuping Xia , Tong Chen , Lai-chan Zhang , Peng Qine , Yongyao Xia,** K-doped $Na_3Fe_2(PO_4)_3$ cathode materials with high-

stable structure for Sodium-ion stored energy battery, Journal of Alloys and Compounds, vol-784, 939-946, 5 May 2019. https://doi.org/10.1021/cm101377h

[42]. A. R. West, Solid State Chemistry and its Applications, Ed. John Wiley and sons, New York (1987) , March 2014, pages-584

[43**]**.https://global.oup.com/ushe/product/crystal-structure-analysis-9780199576357?cc=in&lang=en&

[44].http://biophysics.fsu.edu/soma/wpcontent/uploads/sites/13/2016/10/2016PANalyticalXPertProDataCollection.pdf

[45]. https://aip.scitation.org/doi/abs/10.1063/1.1710298?journalCode=jap

[46] Information on the FESEM (Field-emission Scanning Electron Microscope) Radboud University Nijmegen http://www.sem.com/analytic/sem.htm

[47] https://www.mee-inc.com/laboratory-expertise/field-emission-sem-fesem/

[48].Morphological characterization of Nano particles, Anshida Mayeen, Nandakumar Kalarikkal, in Characterization of Nanomaterials, 2018. http://dx.doi.org/10.1016/B978-0-08-101973-3.00012-2

[49]. https://www.worldcat.org/title/shriver-atkins-inorganic-chemistry/oclc/62326825

[50].https://www.hitachihightech.com/global/products/science/tech/ana/thermal/descriptions/dta.html

[51]. **Anthony R**. West, Basic Solid State Chemistry, 2nd Edition, Wiley, London, 2001, pp. 203-210.https://doi.org/10.1002/(SICI)1099-0739(200004)14

[52]. https://www.gossmanforensics.com/pdf-library/pdf-analytical-methods/thermograv.pdf

[53]. Tyler Salisbury and Jesse white, The Advantages of Thermal Analysis Prior to Bench-Scale Roasting, Drying,roasting and calcining of minerals, pp 27-34, 2015. DOI: 10.1007/978-3-319-48245-3_4

[54]. **Dana E. Moseson, Madison A. Jordan, Dishan D. Shah, Isaac D. Corum, Benedito R. Alvarenga Jr., Lynne S. Taylor** Application and limitations of thermogravimetric analysis to delineate the hot melt extrusion chemical stability processing window,vol-590, 30 November 2020, 119916. https://doi.org/10.1016/j.colsurfa.2019.123957

[55].https://www.mt.com/in/en/home/applications/L1_AutoChem_Applications/Raman-Spectroscopy.html

[56]. Introduction to Raman Spectroscopy and Instrumentation. AZoM. Retrieved on May 03, 2022 from https://www.azom.com/article.aspx?ArticleID=10290.

[57]. **Buzgar N., Apopei A. I., Buzatu A. (2009) – Romanian Database of Raman Spectroscopy (**http://rdrs.ro**)**.

[58]. https://www.ossila.com/en-in/pages/cyclic-voltammetry.

[59].https://chem.libretexts.org/Bookshelves/Analytical_Chemistry/Supplemental_Modules Analytical_Chemistry/Instrumental_Analysis/Cyclic_Voltammetry.

[60].https://www.edaq.com/w/images/5/50/EXP002_Cyclic_Voltammetry_of_Ferrocene_Carboxylic_Acid_PDF.pdf

[61].https://www.researchgate.net/post/What_is_the_limitation_of_Fast_Scan_Cyclic_Voltammetry

[62]. Pavla Hermankova, Martin Hermanek, and Radek Zboril, Thermal Decomposition of Ferric Oxalate Tetrahydrate in Oxidative and Inert Atmospheres: The Role of Ferrous Oxalate as an Intermediate, Eur. J. Inorg. Chem. 2010, 1110–1118. https://doi.org/10.1002/ejic.200900835

[63]. **Masafumi Hiratsuka, Tsuyoshi Honma, Takayuki Komatsu,** Vitrification of maricite $NaFePO_4$ crystal by laser irradiation and enhanced sodium ion battery performance, Journal of Alloys and Compounds 885 (2021) 160928. https://doi.org/10.1016/j.jallcom.2021.160928

[64]. **M. Karthik, S. Sathishkumar , R. BoopathiRaja , K. L. Meganathan , and T. Sumathi,** Design and fabrication of $NaFePO_4$/MWCNTs hybrid electrode material for sodium-ion battery, Journal of material science: Materials in electronics, 31, pages 21792–21801, 2020. https://doi.org/10.1007/s10854-020-04691-y

[65]. **V. Priyanka, R.Subadevi, M.Sivakumar,** Synthesis And Structural Analysis of $NaFePO_4$ Nanocomposite For Sodium Ion Batteries, International Research Journal of Engineering and Technology (IRJET), vol-4, Issue-9, Sep 2017. https://doi.org/10.1016/j.jpowsour.2016.03.003

[66]. **Xudong Ma, Jiuyang Xia, Xuehang Wu, Zhiyi Pan, Pei Kang Shen,** Remarkable enhancement in the electrochemical activity of maricite $NaFePO_4$ on high-surface-area carbon cloth for sodium-ion batteries, carbon 146 (2019), 78-87. https://doi.org/10.1016/j.carbon.2019.02.004

[67]. **Yongjin Fang, Lifen Qian, Xinping Ai, Hanxi Yang, Yuliang Cao**- Mesoporous Amorphous $FePO_4$ Nanospheres as High-Performance Cathode Material for Sodium-Ion Batteries, Nano Lett,2014, 14, 339- 3543. https://doi.org/10.1021/nl501152f

[68]. **Dessie Tibebe, YezbieKassa and Ashok N. Bhaskarwar,** Treatment and characterization of phosphorus from synthetic waste water using aluminum plate electrodes in the electro coagulation process, BMC Chemistry, 13, 107 (2019) https://doi.org/10.1186/s13065-019-0628-1